

Magnetic Holes Upstream of the Martian Bow Shock: MAVEN Observations

Hadi Madanian¹, Jasper, S. Halekas¹, Christian, Xavier Mazelle², Nick Omidi³, Jared, Randolph Espley⁴, David, L. Mitchell⁵, and James P. Mcfadden⁵

¹University of Iowa

²IRAP; Université de Toulouse; CNRS; CNES; UPS-OMP; Toulouse, France

³Solana Scientific Inc

⁴NASA Goddard

⁵University of California, Berkeley

November 21, 2022

Abstract

Magnetic holes (MHs) are pressure-balanced structures characterized by distinct decreases in the interplanetary magnetic field (IMF) strength in otherwise unperturbed solar wind. In this paper we present an analysis of MHs upstream of the Martian bow shock based on three months of observations by the Mars Atmosphere and Volatile Evolution (MAVEN) spacecraft. Plasma properties within and around these structures as well as their shape characteristics are examined. We find an occurrence rate of around 2.1 events per day. About 48 percent of all events are of linear type with magnetic field rotation across the hole less than 10 degrees. We observe linear magnetic holes both as isolated events and as part of a train of magnetic holes. The proton temperature anisotropy inside MHs increases while alpha particles remain mostly isotropic. The average electron temperature inside MHs modestly increases with increasing hole depth. The duration of linear holes at 1.5 AU shows an increase compared to durations at smaller heliocentric distances, but the structures remain asymmetrical and ellipsoid. A case study of MHs accompanied by a population of heavy pickup ions is also discussed.

Magnetic Holes Upstream of the Martian Bow Shock: MAVEN Observations

H. Madanian¹, J. S. Halekas¹, C. Mazelle², N. Omidi³, J. R. Espley⁴, D. L.
Mitchell⁵, J. P. McFadden⁵

¹Department of Physics and Astronomy, University of Iowa, Iowa City, IA, USA.

²L'Institut de Recherche en Astrophysique et Planétologie, CNRS, Université de Toulouse, UPS, CNES,
France.

³Solana Scientific Inc., Solana Beach, CA, USA.

⁴NASA Goddard Space Flight Center, Greenbelt, Maryland, USA

⁵Space Sciences Laboratory, University of California, Berkeley, California, USA.

Key Points:

- Linear and rotational magnetic holes are observed in the solar wind upstream of Mars
- Proton temperature anisotropy inside the holes increases while alpha particles remain mostly isotropic
- Pickup ions create an environment favorable for generation of mirror mode structures upstream of the bow shock

Corresponding author: Hadi Madanian, hadi-madanian@uiowa.edu

Abstract

Magnetic holes (MHs) are pressure-balanced structures characterized by distinct decreases in the interplanetary magnetic field (IMF) strength in otherwise unperturbed solar wind. In this paper we present an analysis of MHs upstream of the Martian bow shock based on three months of observations by the Mars Atmosphere and Volatile Evolution (MAVEN) spacecraft. Plasma properties within and around these structures as well as their shape characteristics are examined. We find an occurrence rate of around 2.1 events per day. About 48 percent of all events are of linear type with magnetic field rotation across the hole less than 10 degrees. We observe linear magnetic holes both as isolated events and as part of a train of magnetic holes. The proton temperature anisotropy inside MHs increases while alpha particles remain mostly isotropic. The average electron temperature inside MHs modestly increases with increasing hole depth. The duration of linear holes at 1.5 AU shows an increase compared to durations at smaller heliocentric distances, but the structures remain asymmetrical and ellipsoid. A case study of MHs accompanied by a population of heavy pickup ions is also discussed.

Plain Language Summary

The solar wind, a supersonic flow of electrons and ions flowing radially outward from the Sun, carries a magnetic field. Magnetic holes are structures with reduced magnetic field strength that last between a few seconds to a few minutes. These structures have been observed at many places throughout the solar system. A common formation mechanism for magnetic holes is a wave mode instability that converts magnetic energy into ion thermal energy, known as the mirror mode. Mirror mode instabilities grow when the temperature of ions moving perpendicular to the magnetic field is higher than that of ions moving in the parallel direction. Mirror waves alter the magnetic field and the spatial structure of the plasma. In this paper, we use observations from the MAVEN spacecraft to study magnetic holes in the space environment around Mars.

1 Introduction

Solar wind magnetic holes (MHs) or magnetic decreases are structures characterized by distinct depressions in the interplanetary magnetic field (IMF) strength anticorrelated with plasma density variations (Turner et al., 1977; Tsurutani et al., 1992; Stevens & Kasper, 2007). MHs have been observed throughout the solar system at Mercury (Karlsson

49 et al., 2016), Venus (Zhang, Russell, Baumjohann, et al., 2008; Zhang, Russell, Zambelli,
 50 et al., 2008), 1 AU (Fitzenreiter & Burlaga, 1978; Chisham et al., 2000; Zurbuchen et
 51 al., 2001; Stevens & Kasper, 2007; Xiao et al., 2010; Balikhin et al., 2010), over a range
 52 of heliocentric distances (Burlaga et al., 2006, 2007; Fränz et al., 2000; Sperveslage et
 53 al., 2000; Winterhalter et al., 1995; Tsurutani et al., 2009) and solar latitudes (Fränz et
 54 al., 2000; Tsurutani et al., 2011; Winterhalter et al., 2000). Based on the rotation of the
 55 magnetic field across the structure, magnetic holes are classified as linear holes (when
 56 there is no or a small rotation), and rotational holes (for rotations greater than $\sim 30^\circ$).
 57 No definite argument against or in favor of a rotation angle limit has so far been pro-
 58 posed and different authors have chosen different angles to categorize linear MHs in their
 59 observations (e.g., rotations below 15° in Xiao et al. (2010), and below 5° in Fränz et
 60 al. (2000)). The rotational holes are associated with a current sheet and are considered
 61 a subset of directional discontinuities which do not require a field reduction (Smith, 1973).

62 Turner et al. (1977) estimated an occurrence rate of 1.5 per day for these struc-
 63 tures at 1 AU. Through a multi-spacecraft analysis using Helios 1, 2 and Voyager 2 space-
 64 craft data, Sperveslage et al. (2000) investigated the heliocentric radial dependence of
 65 MH occurrence rate between 0.3 AU and 17 AU. The occurrence rate remains constant
 66 within 1 AU, but decreases beyond 2 AU with increasing heliocentric distance, with no
 67 clear radial dependence observed between 1 and 2 AU. Out of 850 MHs in the Sperveslage
 68 et al. (2000) study, nearly 30% were linear holes, a rate much higher than the 13% rate
 69 observed in Ulysses data in the ecliptic plane (Tsurutani et al., 2009). Other studies at
 70 1 AU have reported $\sim 39\%$ of all magnetic holes are of linear type (Briand et al., 2010;
 71 Stevens & Kasper, 2007), while over the solar poles nearly half of the magnetic depres-
 72 sions are linear MHs (Fränz et al., 2000; Tsurutani et al., 2011). Both types of MHs have
 73 been observed at Venus. Zhang, Russell, Zambelli, et al. (2008) examined solar wind data
 74 from the Venus Express spacecraft for magnetic holes identified as the minimum field
 75 strength within a 300 s rolling window with at least 50% decrease below the background
 76 field, and found that at 0.72 AU the duration of rotational holes associated with a re-
 77 connection current sheet is generally less than 30 s and their thickness is about 2000 km,
 78 comparable to observations at 1 AU.

79 Magnetic holes occur in a variety of time scales from seconds to minutes (Fränz et
 80 al., 2000; Stevens & Kasper, 2007; Zurbuchen et al., 2001). These time scales correspond
 81 to tens of local proton gyroradii in spatial scale, which makes these structures kinetic-

82 scale phenomena. Several mechanisms have been proposed for the generation of MHs (or
83 magnetic depressions). A substantial number of studies have considered the mirror mode
84 instability as the likely formation mechanism of linear MHs (Tsurutani et al., 1992; Win-
85 terhalter et al., 1995; Stevens & Kasper, 2007; Burlaga et al., 2006). Mirror mode waves
86 grow in high β (the ratio of the plasma thermal pressure to the magnetic pressure) plasma
87 with temperature anisotropy $T_{\perp}/T_{\parallel} > 1$, where \perp and \parallel denote directions perpendic-
88 ular and parallel to the background magnetic field, respectively. The temperature anisotropy
89 serves as a source of free energy for particles to nonlinearly interact with magnetic field
90 perturbations (Southwood & Kivelson, 1993; Tajiri, 1967; Hasegawa, 1969; Kivelson &
91 Southwood, 1996). Mirror mode instabilities have been frequently observed in terrestrial
92 and planetary magnetosheaths where shock compression and field line draping cause per-
93 pendicular ion heating that provides favorable conditions for mirror mode instabilities
94 to develop (Califano et al., 2008; Erdős & Balogh, 1996; Hubert & Harvey, 2000; Joy et
95 al., 2006; Lucek et al., 2001; Soucek et al., 2008; Tsurutani et al., 2011). Pickup ions pro-
96 duced through ionization of neutral particles in the extended planetary exosphere can
97 also cause mirror instability in plasma. These ions are accelerated by the solar wind mo-
98 tional electric field perpendicular to IMF, introducing temperature anisotropy to the so-
99 lar wind plasma (Szegö et al., 2000; Wu & Davidson, 1972). As such, pickup ions are con-
100 sidered the main source of mirror mode wave generation in the heliosheath and in cometary
101 environments (Burlaga et al., 2007; Liu et al., 2007; Russell et al., 1987; Volwerk et al.,
102 2016; Glassmeier et al., 1993). A comprehensive review by Tsurutani et al. (2011) de-
103 scribed a classification scheme to distinguish mirror modes from magnetic decreases in
104 which, mirror mode structures are considered quasi-periodic, while magnetic decreases
105 are variable-scale and non-periodic features. In our study, the terms magnetic holes and
106 magnetic depressions/decreases are used interchangeably. Other mechanisms for gener-
107 ation of MHs include, large-amplitude polarized Alfvénic waves (Buti et al., 2001), mag-
108 netic reconnection in the high corona (Zurbuchen et al., 2001), the ponderomotive force
109 of phase steepened Alfvén waves (Tsurutani et al., 2002), and dark solitons in the so-
110 lar wind (Baumgärtel, 1999). In addition, an early theoretical kinetic framework devel-
111 oped by Lemaire and Burlaga (1976) aimed at explaining diamagnetic effects in the bound-
112 ary layer of tangential discontinuities based on the kinetic properties of electrons and ions
113 (Burlaga & Lemaire, 1978).

114 In this paper we aim to investigate magnetic holes upstream of Mars' bow shock
 115 at 1.5 AU and examine various characterizing plasma properties of these structures. We
 116 focus on small timescale magnetic depressions lasting less than a few minutes. The pa-
 117 per is structured as follows. In section 2 we describe the instrumentation and available
 118 data, in section 3 the event identification method is discussed, plasma conditions and vari-
 119 abilities of magnetic holes are presented in section 4, and in section 5 conclusions and
 120 implications are given.

121 **2 Instrumentation and Data Processing**

122 The MAVEN spacecraft was launched in November 2013 and was designed to mea-
 123 sure the energy and particle input from the Sun into the Mars upper atmosphere (Jakosky
 124 et al., 2015). The spacecraft has an inclined elliptical orbit with a nominal altitude of
 125 150 km at the periapsis, and 6220 km at the apoapsis. Each orbit is ~ 4.5 hours and thanks
 126 to the orbital precession, observations cover a variety of local times, altitudes, and lat-
 127 itudes. Orbit properties changed slightly in Spring of 2019 (and still evolving) as the aer-
 128 obraking phase of the mission started. All data used in this study are from level-2 cal-
 129 ibrated data products. Magnetic field data are from the magnetometer system which con-
 130 sists of two fluxgate sensors mounted at two opposite ends of the solar arrays (Connerney
 131 et al., 2015). The sensors measure ambient magnetic field with a resolution of 0.008 nT
 132 and an accuracy of 0.05%. Magnetic field measurements have been averaged to a 1 s re-
 133 solution. Ion measurements are from the Solar Wind Ion Analyzer (SWIA) instrument
 134 (Halekas et al., 2015). SWIA is an energy analyzer that measures ions with energies be-
 135 tween 25 eV to 25 keV over a wide field-of-view (FOV) (360° azimuth \times 90° polar) cov-
 136 ered by 10 fine anodes, each 4.5° wide, in the solar wind direction plus 14 wider anodes,
 137 each 22.5° , covering the rest of the azimuthal plane. The polar angles (-45° , $+45^\circ$) are swiped
 138 by electrostatic deflections, with 24 deflection steps at each energy bin, resulting in a 3.75°
 139 available resolution. Depending on the plasma environment and operation mode, SWIA
 140 returns data with different energy and angular resolutions. In the "fine" mode, 3D
 141 distributions are limited to energy bins and FOVs near the peak of the distribution. This
 142 is the default operation mode in the solar wind and has $7.5\% \times 3.75^\circ \times 4.5^\circ$ energy and
 143 angular resolutions. In the "coarse" mode, distributions have smaller resolutions (15%
 144 $\times 22.5^\circ \times 22^\circ$) but cover almost all FOVs and energies. The time resolution of returned
 145 3D distributions is 8 s. A set of ion moments (density, velocity, and temperature) is also

146 available that is calculated onboard from the current mode measurements. We use the
 147 fine mode data to derive ion moments for protons and alpha particles separately for higher
 148 accuracy. This is accomplished by estimating the ion energy at the peak of each distri-
 149 bution (i.e., proton energy), and dissecting the energy spectrum. To find moments in the
 150 magnetic field-aligned coordinates, the pressure tensor is first calculated in the instru-
 151 ment frame and then rotated into the magnetic field-aligned coordinates. This leads to
 152 two perpendicular terms in the diagonalized matrix of which, the higher term is adopted
 153 (for more details see section 2 in Halekas, Brain, et al. (2017)). The solar wind ion en-
 154 ergy spectra at times may show ion populations below the nominal proton energy. These
 155 ions are associated with solar wind ions scattered from the SWIA instrument harness-
 156 ing or spacecraft body, and most of them are excluded from the FOV and energy range
 157 in the fine mode and thus have negligible effects on our ion moment analysis. SWIA mea-
 158 surements are used in conjunction with the SupraThermal and Thermal Ion Composi-
 159 tion (STATIC) instrument, an electrostatic analyzer combined with a time-of-flight mod-
 160 ule (McFadden et al., 2015). STATIC can resolve dominant ion species (H^+ , He^+ , He^{++} ,
 161 O^+ , O_2^+ , CO_2^+) in the Martian atmosphere and magnetosphere. STATIC has a similar
 162 angular coverage to SWIA; however, its energy resolution in the solar is less. The 'c6'
 163 data product of STATIC with 32 energy channels and 64 mass bins provides the most
 164 relevant data for our study. Distributions in this mode are summed over all FOVs. Elec-
 165 tron density and temperature are measured by the Solar Wind Electron Analyzer (SWEA)
 166 instrument (Mitchell et al., 2016). SWEA is also an electrostatic analyzer that measures
 167 electrons in the 3 - 4600 eV energy range, with an energy resolution of $\Delta E/E \sim 17\%$.
 168 The temporal resolution of SWEA data is 2 s. SWEA data are corrected for the FOV
 169 blocking by the spacecraft body, background noise, and spacecraft potential that is usu-
 170 ally slightly positive in the solar wind. Electron densities and temperatures are calcu-
 171 lated from 1D moments by assuming an isotropic electron distribution.

172 **3 Event Identification**

173 We focused on three months of MAVEN observations between 1 June and 1 Septem-
 174 ber 2016 when the MAVEN orbital apoapsis was on the dayside and precessed around
 175 the subsolar point, resulting in the spacecraft spending a substantial fraction of each or-
 176 bit in the solar wind. We used a modeled bow shock boundary, a conic shape determined
 177 from an ensemble of Phobos 2 and Mars Global Surveyor data sets (Trotignon et al., 2006),

178 to identify solar wind segments of each orbit. An alternative way to select solar wind mea-
 179 surements would be to check a combination of criteria on the solar wind bulk flow ve-
 180 locity, ion temperature, and magnetic field fluctuations (Halekas, Ruhunusiri, et al., 2017).
 181 But since we are searching for field depressions that are isolated and have relatively large
 182 δB , that may not be the best approach for our purposes. To identify magnetic depres-
 183 sions we follow a similar method to Zhang, Russell, Baumjohann, et al. (2008) and Plaschke
 184 et al. (2018), with some modifications in the criteria to adapt them to MAVEN obser-
 185 vations. We start with 1 Hz magnetic field data and calculate the depression time-series
 186 from $\Delta B/B = (B_i - B_{bg})/B_{bg}$, where B_i is the magnetic field magnitude at each point
 187 and B_{bg} (Background field) is the average magnetic field magnitude over a 150 s rolling
 188 interval. We scan the time-series, one point at a time, for minimum depressions within
 189 the rolling window. Once a minimum depression point is found, we check the following
 190 criteria: (1) $\Delta B/B$ should be less than $d_{th} = -0.35$, (2) one minute before and after
 191 the event, the standard deviation in magnetic field magnitudes, σ_B , should not exceed
 192 half of σ_B of the event interval, (3) the average magnetic field strengths one minute be-
 193 fore and after the event should be within two standard deviations of one another; (4) the
 194 average plasma density, n , at the event time should not be less than one standard de-
 195 viation of densities one minute before or after the event ($\bar{n}_{event} \geq \bar{n}_{before,after} - \sigma_{before,after}$).

196 An example of the search algorithm for a MH event on 15 August 2016 at 21:37:47
 197 UTC is shown in Figure 1. In this figure, three components of the magnetic field in the
 198 Mars-centered Solar Orbital (MSO) coordinate are shown in panels (a)-(c). The MSO
 199 frame origin is at Mars ' center-of-mass with the $+X$ axis pointing to the Sun, the Z
 200 axis perpendicular to the ecliptic plane with $+Z$ pointing above the plane, and the Y
 201 axis completing the right-hand coordinate system (roughly anti-parallel to the Mars or-
 202 bital velocity). The solid line in panel (d) represents the field strength, B , and the back-
 203 ground field (B_{bg}) is shown with the dashed line. Panel (e) shows the depression time-
 204 series. The horizontal dashed-dotted line is drawn at -0.35 , the depression threshold d_{th} .
 205 The two vertical dashed lines mark the start and end times determined as the nearest
 206 points to the minimum depression when the depression recovers and reaches $0.1 * d_{th}$.

207 The boundaries could also be identified as the nearest points with magnetic field
 208 magnitude larger than $B_{bg} - \sigma_B$, where σ_B is the standard deviation of magnetic field
 209 magnitude at event time. Both methods lead to identical boundaries for the majority

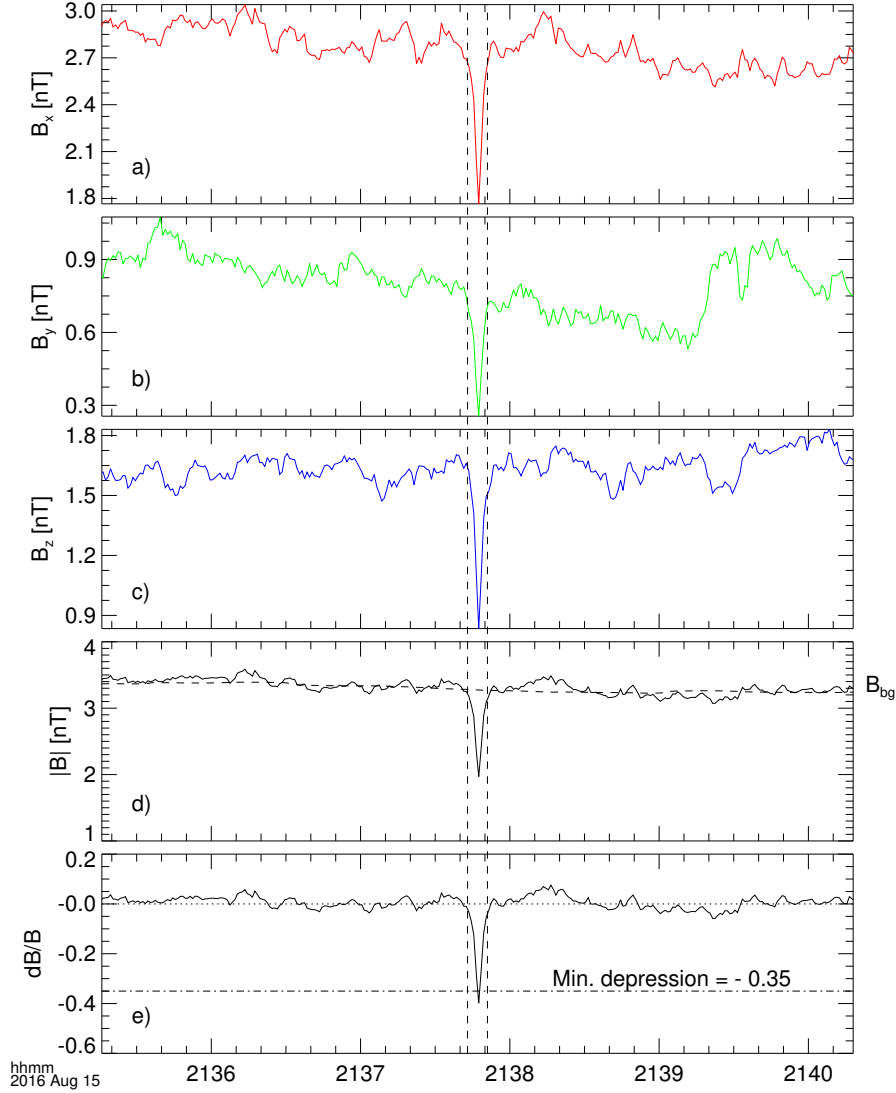


Figure 1. Magnetic hole event at 21:37:47 UTC on 15 August 2016. Panels (a)-(c) show the three components of the magnetic field in the MSO coordinate. The solid line in panel (d) shows the field strength B and the background field strength (B_{bg}) is indicated by the dashed line. B_{bg} is the averaged field strength over a 150 s window centered on the minimum depression point. Panel (e) shows the depression levels. The dashed dotted line at -0.35 is the minimum depression threshold (d_{th}). The two vertical dashed lines mark the the event boundaries determined when the depression reaches -0.035 (i.e. 10% of the threshold value).

210 of events, but for some events with asymmetrical field profiles around the minimum de-
 211 pression, setting a fixed threshold produced more precise boundaries.

212 The minimum depression threshold in criterion 1 is an empirical value, which pro-
 213 vides adequate identification of MHs while minimizing false positive events. Reducing
 214 this threshold leads to more positive events, but at the expense of an increased risk of
 215 detecting random variations that are not MHs. Restricting σ_B before and after the event
 216 in criterion 2 increases the chance of selecting well-defined events. Criterion 3 eliminates
 217 step-like events, which commonly occur during shock crossings, foreshock compressional
 218 boundaries, and Short Large Amplitude Magnetic Structures (SLAMS) (Schwartz & Burgess,
 219 1991; Omidi et al., 2009; Halekas, Ruhunusiri, et al., 2017). The main difference between
 220 our identification method and that of previous studies is criterion 4 which was imple-
 221 mented after finding many transient foreshock events in our initial event set. Hot Flow
 222 Anomalies (HFAs), Spontaneous HFAs, and foreshock cavities are among the foreshock
 223 transient structures that are characterized by correlated magnetic field strength and plasma
 224 abundance variations (Sibeck et al., 2004; Schwartz et al., 2006; Omidi et al., 2013; Omidi
 225 & Sibeck, 2007; Collinson et al., 2015, 2017). Some of these structures are associated with
 226 Ultra-low frequency (ULF) waves. As the solar wind interacts with a bow shock, some
 227 solar wind ions are reflected back upstream by the potential difference across the bow
 228 shock. The backstreaming ions move sunward in the solar wind frame with velocities in
 229 the order of a few Alfvén speed and interact with the incident solar wind, driving non-
 230 linear ion-ion instabilities that lead to generation of ULF waves (Gary et al., 1981; Hoppe
 231 & Russell, 1983; Halekas, Brain, et al., 2017; Mazelle et al., 1991; Gary, 1993). In ad-
 232 dition, fluid models of the mirror mode instability have shown that energy exchange be-
 233 tween parallel and perpendicular particle flux and field components drives the plasma
 234 out of the high magnetic field region and into the magnetic holes with decreased field
 235 causing increased plasma densities inside the holes (Southwood & Kivelson, 1993), which
 236 further supports inclusion of criterion 4. Stevens and Kasper (2007) classified magnetic
 237 holes found through this type of search algorithm as "young holes" which are near
 238 saturation and closer to the instability threshold. We performed the search with 300 s
 239 and 500 s windows to avoid any biases due to the shifting window size. Finally, events
 240 are visually inspected to ensure that all events are well-defined magnetic holes.

241 4 Observations

242 Figure 2 illustrates four examples of magnetic field profile across magnetic holes.
 243 Each event is presented within a 6-minute timespan. Panel (a) shows two magnetic holes

244 on 29 June 2016 separated by about one minute. The first depression at 04:50:55 UTC
 245 is more symmetric compared to the event at 04:52:00 UTC which possesses more struc-
 246 tures in the middle (i.e., a nested hole). The second panel shows a MH at 20:54:36 UTC
 247 on 9 July, where recovery from the minimum depression occurs in two steps. There is
 248 also a smaller hole at around 20:53:25 UTC which does not meet the minimum depres-
 249 sion requirement. These two events are also separated by about one minute. The mag-
 250 netic field strength in the event on the third panel decreases by 84% and the structure
 251 is symmetrical, while the IMF surrounding the hole is very quiet.

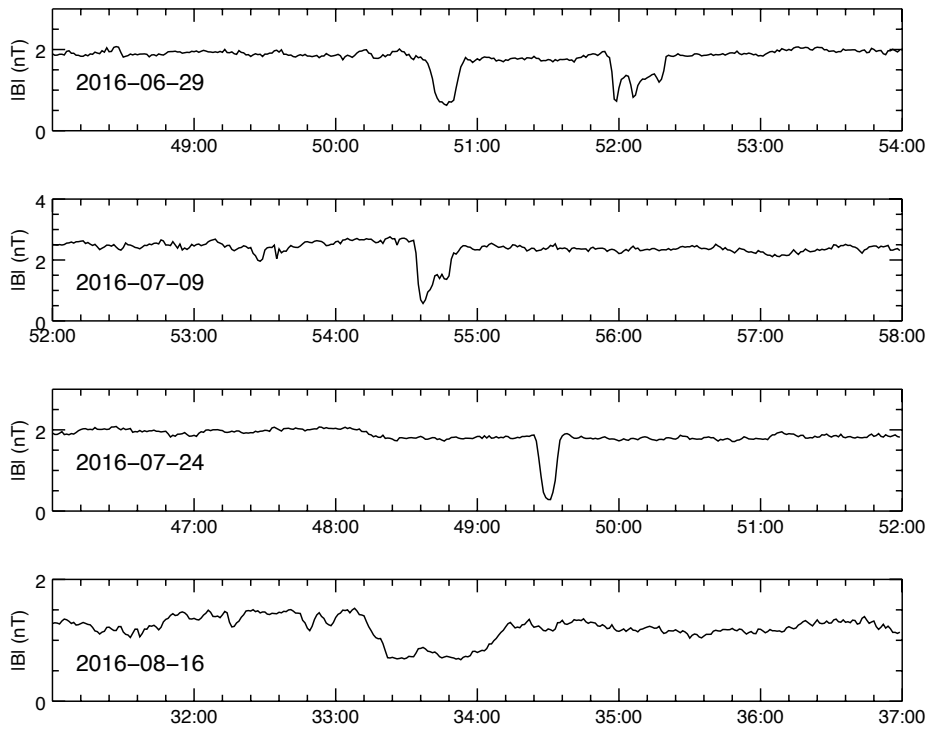


Figure 2. Four examples of magnetic field profile around MHs observed by MAVEN. Event dates are annotated on each panel. The horizontal axes indicate the UTC time.

252 The relatively long MH in the fourth panel occurred on 16 August 2016 between
 253 15:33:10 and 15:34:12 UTC. The shape of this event is rather different than the previ-
 254 ous examples. The boundaries are extended over a longer period and the depression is
 255 plateaued at around 0.7 nT and shows a peak near the center of the hole.

256

4.1 Statistical Analysis of Magnetic Holes

257

258

259

260

261

262

263

264

265

266

267

From three months of data used in our analysis we obtain 102 events which gives an occurrence rate of about 2.1 events per day considering that the spacecraft spent, on average, 55% of each orbit in the solar wind. The spatial distribution of events around Mars is shown in Figure 3 which illustrates a cylindrical projection of events. The axes are in units of Mars radii (R_M). Mars (in yellow) is at the origin and the meshed surface represents the modeled bow shock boundary. Events are spread along the spacecraft trajectory in the solar wind and do not show any particular pattern with respect to event duration, depth, or type. Some events appear very close to the bow shock, though they are still in the solar wind flow. For instance, for the event located on the boundary at $X_{SMO} \sim 1 R_M$ the solar wind speed is ~ 490 km/s and the dynamic pressure ~ 2 nPa, which could displace the bow shock further inward than the model predicted.

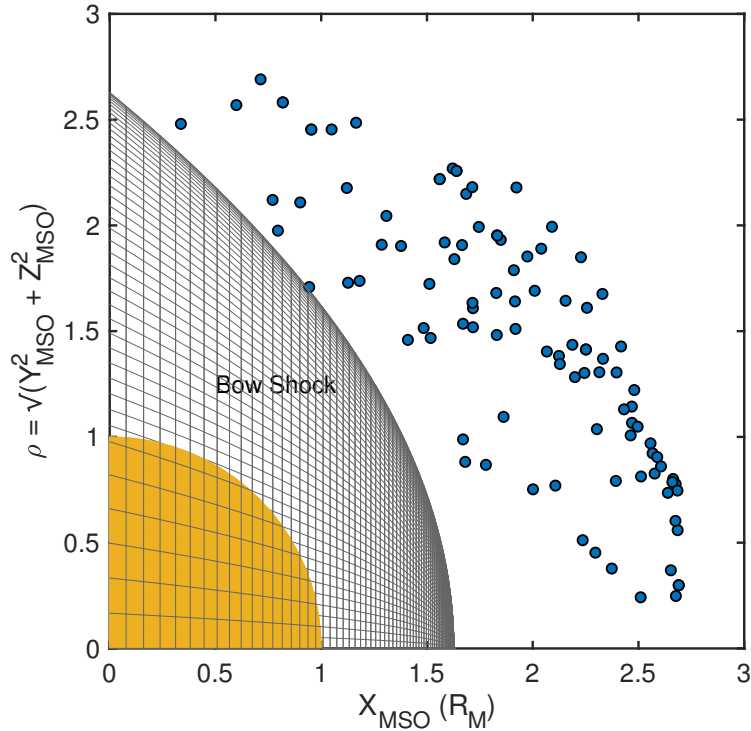


Figure 3. Distribution of magnetic holes upstream of the Martian bow shock in cylindrical coordinates. The axes are in units of Mars radii (R_M).

268

269

270

Once event boundaries have been determined, plasma parameters including, proton and alpha particle temperature, anisotropy, density, solar wind bulk flow speed, electron density and temperature during the event and in the adjacent solar wind are recorded.

271 We also calculate the magnetic field rotation, $\Delta\varphi$, across the holes using the magnetic
 272 field vectors at the start and end times. Panel (a) in Figure 4 shows the occurrence rate
 273 distribution of $\Delta\varphi$ which varies between 0.3° and 172° . The most probable rotation an-
 274 gles lies between 5° - 10° . Around $\sim 48\%$ of events are linear MHs ($\Delta\varphi < 10^\circ$). The event
 275 duration distribution in panel (b) shows an exponential decrease for events longer than
 276 10 s. The median event duration is ~ 19 s, and ~ 15.5 s for linear holes. From event du-
 277 rations and the corresponding solar wind bulk flow velocity and proton temperature, we
 278 estimate the spatial scale size of events along the solar wind flow. Panel (c) in Figure
 279 4 represents the scale size distribution per local proton gyroradii, r_ρ , calculated from the
 280 average magnetic field magnitude inside the holes. For rotational holes this size is a mea-
 281 sure of the current sheet thickness. The distribution in panel (c) also shows an exponen-
 282 tial pattern for structures larger than $15 r_\rho$. Similar exponential distributions have been
 283 reported in previous statistical studies of MHs at 1 AU (Stevens & Kasper, 2007; Tsuru-
 284 rutani et al., 2011).

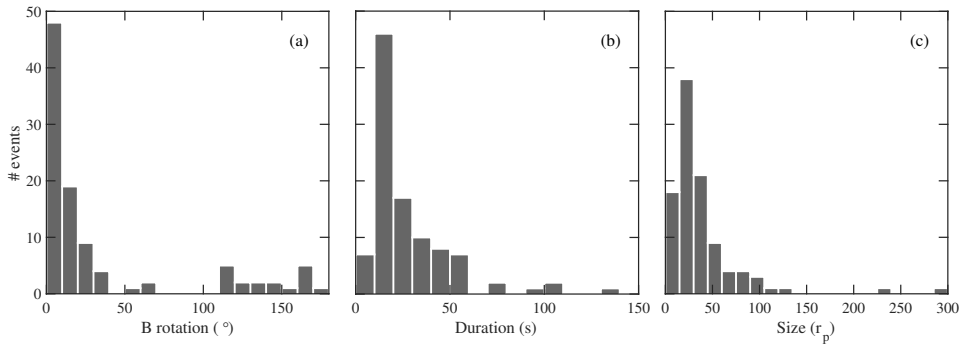


Figure 4. Occurrence rate distribution of (a) rotation of magnetic field across magnetic holes ($\Delta\varphi$), (b) event duration, (c) event size normalized in local proton gyroradii (r_ρ).

285 For linear magnetic holes the stability condition parameter R provides an estimate
 286 of whether mirror mode waves can develop in the plasma (Hasegawa, 1969; Winterhal-
 287 ter et al., 1994), and is defined by:

$$R = \frac{\beta_\perp}{\beta_\parallel} \frac{1}{1 + \frac{1}{\beta_\perp}} \quad (1)$$

288 where $\beta_{\perp,\parallel}$ are the plasma betas calculated inside the holes,

$$\beta_{\perp,\parallel} = \frac{(n_p T_{p\perp,\parallel} + n_\alpha T_{\alpha\perp,\parallel}) k_b}{B^2 / 2\mu_0} \quad (2)$$

289 n_p and n_α are the proton and alpha particle densities, respectively, k_b is the Boltzmann
 290 constant, μ_0 is the vacuum permeability constant, and T represents the corresponding
 291 ion temperatures. For $R > 1$, plasma is unstable and mirror mode waves can grow, while
 292 for values close to 1, plasma is considered marginally stable. The underlying particle dis-
 293 tribution that drives this particular form of instability threshold is bi-Maxwellian. Non-
 294 Maxwellian distributions such as suprathermal ion tail, and anisotropic electron distri-
 295 butions both increase the pressure anisotropy and act to lower the instability threshold
 296 (Pokhotelov, 2002). The distribution histogram in Figure 5 shows the distribution of the
 297 highest instability parameter value for linear holes. The majority of the 49 linear holes
 298 are either unstable or only marginally stable (31 events show $R > 1$).

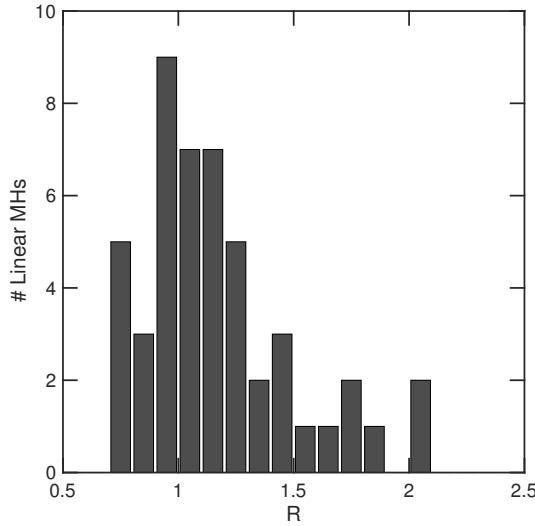


Figure 5. Histogram distribution of instability condition R for linear MHs with $\Delta\varphi < 10^\circ$.

299 The solar wind proton perpendicular temperature inside the magnetic holes increases
 300 from its value in the ambient solar wind (Fränz et al., 2000; Neugebauer et al., 2001; Tsu-
 301 rutani, 2002). In panels (a) and (b) of Figure 6 we show histograms of inside-to-outside
 302 ratios of solar wind ion temperature perpendicular and along the local magnetic field,
 303 respectively. All 102 events are included in this figure. Proton temperature variations
 304 (blue bars) predominantly occur in perpendicular direction. Most events exhibit higher
 305 perpendicular proton temperature inside the hole, confirming the findings of previous

306 studies. The parallel temperature of protons also increases, but to a lesser degree. For
 307 alpha particles (red bars) the distributions are relatively symmetric, indicating that the
 308 alpha particles remain mostly isotropic.

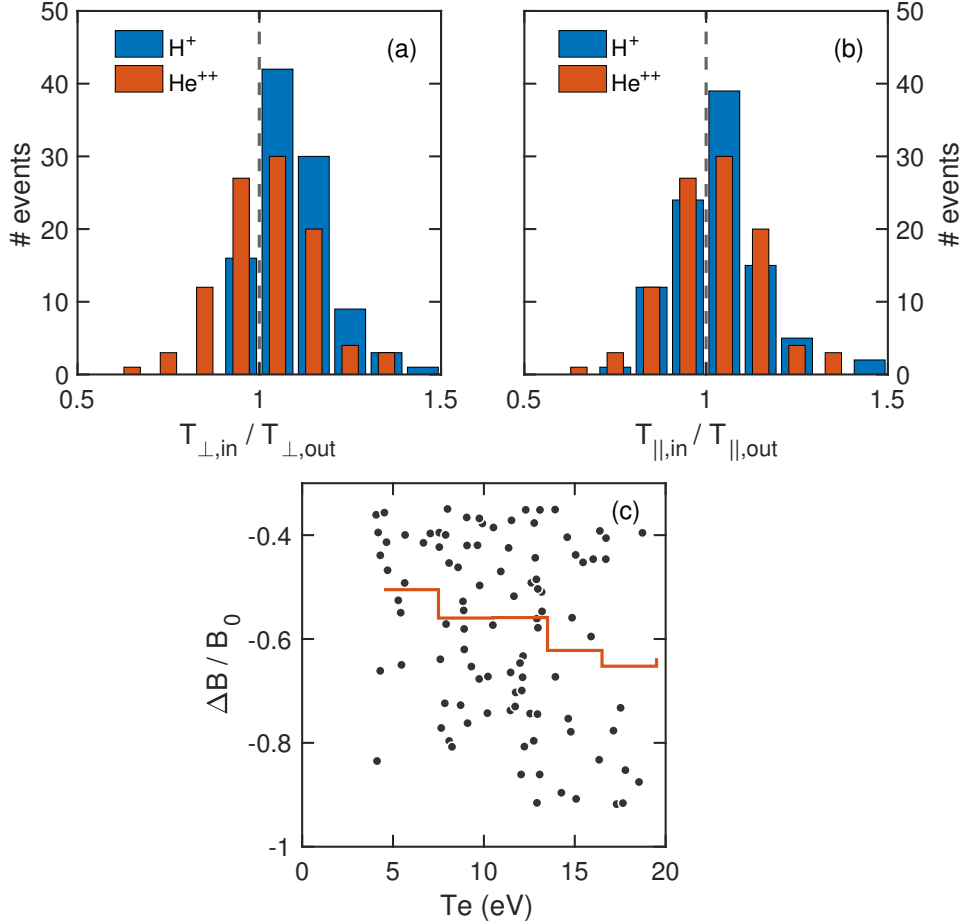


Figure 6. (a) Histogram of inside-to-outside ratios of solar wind protons (blue) and alpha particles (red) perpendicular temperature, (b) histogram of parallel temperature ratios, (c) distribution of event depressions as a function of electron temperature inside the holes. The red lines on panels(c) shows average depression depths in 3 eV temperature bins.

309 The hole depth ($\Delta B / B_{bg}$) distribution as a function of electron temperature is shown
 310 in panel (c) of Figure 6. The red line on this panel represents the averaged depths in 3
 311 eV temperature bins. The electron temperature shows a modest increasing trend at higher
 312 magnetic depressions. Note that our assumption here is that electrons inside MHs are
 313 isotropic ($T_{e\perp} \approx T_{e\parallel}$) (Balikhin et al., 2012; Briand et al., 2010).

314 MHS associated with mirror mode instabilities are non-propagating in the plasma
 315 frame, and structures are extended along the background magnetic field. It has been shown
 316 that a typical magnetic hole at 0.72 AU has an asymmetrical shape in the form of a ro-
 317 tational ellipsoid with major to minor axes ratio of 2.45:1 (Zhang, Russell, Baumjohann,
 318 et al., 2008). A separate analysis at 1 AU showed a consistent shape with the elonga-
 319 tion ratio of 1.84:1, suggesting that MHS develop inside 0.72 AU and their shape is pre-
 320 served in the solar wind (Xiao et al., 2010; Ala-Lahti et al., 2018; Baumgärtel, 1999). While
 321 Burlaga et al. (2007) showed that the normalized size of MHS in the heliosheath is of the
 322 same order of magnitude as their size at 1 AU.

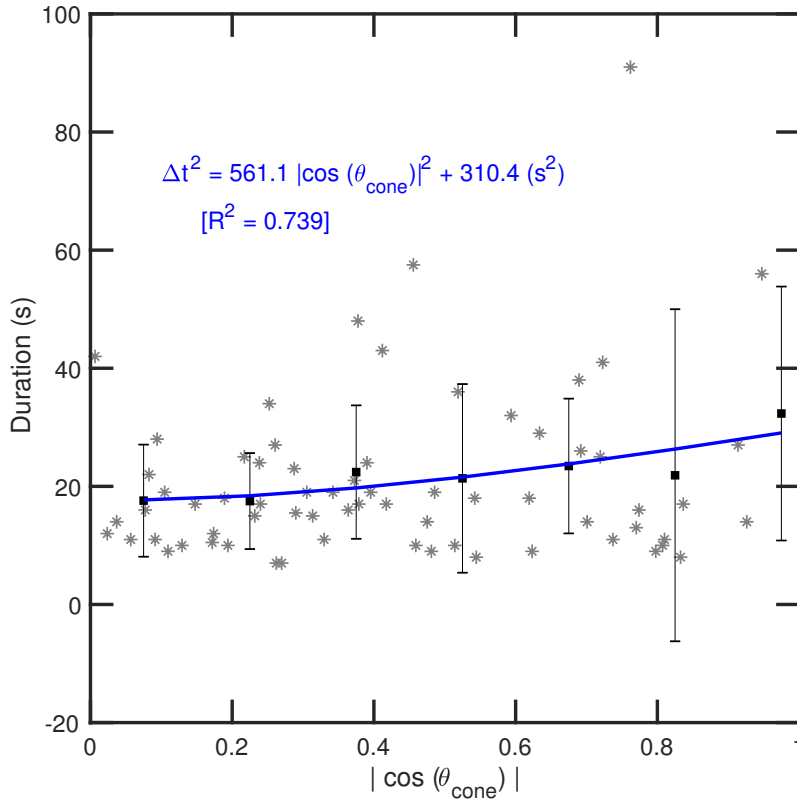


Figure 7. Magnetic hole duration as a function of background field orientation with respect to the solar wind flow. Only holes with $\Delta\varphi < 20^\circ$ are shown. Black squares show average values of the binned data. The blue line is the best fit on the squares describing the shape of a typical structure. The best fit function and the R^2 goodness-of-fit value are annotated in blue. Error bars indicate 1 standard deviation.

323 These observations suggest that there is a consistency in the shape of MHS throughout
 324 the interplanetary medium. Here, we attempt to estimate the typical shape of MHS at

325 1.5 AU using MAVEN data. Figure 7 shows MH durations as a function of IMF orien-
 326 tation with respect to the solar wind flow (i.e., $\cos(\theta_{cone})$, where θ_{cone} is the IMF cone
 327 angle at the beginning of each event). In this figure, asterisks represent 68 MH events
 328 with magnetic field rotation $\Delta\varphi < 20^\circ$, black squares show average durations of data
 329 in $0.15*|\cos(\theta_{cone})|$ bins with error bars indicating 1 standard deviation, and the blue
 330 curve shows a hyperbola fit on the squares in the form of $\Delta t^2 = 561.1|\cos(\theta_{cone})|^2 +$
 331 310.3 (s²). The goodness-of-fit is 0.739. From this equation, two characteristic times for
 332 magnetic field fully radial ($|\cos(\theta_{cone})| = 1$) and fully perpendicular to the flow ($|\cos(\theta_{cone})| =$
 333 0) are estimated that show the typical dwell time for the spacecraft inside linear mag-
 334 netic holes at 1.5 AU are ~ 29.5 s along, and 17.6 s across the magnetic field. At 1.5 AU,
 335 the ratio of structure scale size along and across the magnetic field is about 1.67 (1.43
 336 - 1.75):1.

337 4.2 Train of Magnetic Holes in the Solar Wind

338 Linear MHs are observed both as part of trains of holes or as isolated single events.
 339 Figure 8 shows an example of a train of MHs. Panel (a) in this figure shows the ion en-
 340 ergy spectrogram from SWIA 3D coarse distributions between 100 eV – 7000 eV. The
 341 color bar represents the energy flux in logarithmic scale. The solar wind proton and al-
 342 pha particle beams are recognizable at ~ 850 eV and 1700 eV, respectively. Ion fluxes
 343 below the proton energy are associated with scattered solar wind ions (see section 2).
 344 Panel (b) shows magnetic field data in the MSO frame. Panel (c) shows the plasma den-
 345 sity with an average proton density of ~ 3.8 cm⁻³. The proton temperature shows fluc-
 346 tuations between 5 – 6.5 eV, though no clear relation with magnetic field fluctuations
 347 is observed. Protons show a consistent temperature anisotropy at ~ 1.5 in panel (e), while
 348 alpha particles (not shown) remain roughly isotropic. The instability parameter R in panel
 349 (f) is greater than 1 for the entire period. It seems that for magnetic hole trains the plasma
 350 is consistently unstable both inside and outside the depressions. All MHs in Figure 8 are
 351 linear. Linear MHs generated by mirror mode waves are stretched along the field line.
 352 To check the variations in the magnetic field frame, we performed the minimum variance
 353 analysis (MVA) on the magnetic field data. Panel (g) on this figure shows the principal
 354 magnetic field components B_1 , B_2 , and B_3 along the maximum (orange), intermediate
 355 (cyan), and minimum (black) variance vectors. The ratio of intermediate to minimum
 356 eigenvalues is about 3.4 and the maximum to intermediate ratio is greater than 8, which

357 indicate that the MVA is well conditioned. The maximum variance vector B_1 maintains
 358 the most variations, thereby the magnetic field varies primarily in one direction. The hor-
 359 izontal axis labels at the bottom represent altitude in units of km, surface latitude, sur-
 360 face longitude, and time (hh:mm), respectively. An important signature for the identi-
 361 fication of mirror mode structures is an anticorrelation between the magnetic field strength
 362 and plasma density (Stevens & Kasper, 2007). We observe this anticorrelation in almost
 363 all holes (vertical dashed lines).

364 Mirror mode instabilities can also create magnetic peaks, characterized by local en-
 365 hancements of magnetic field strength and decreased plasma density. Numerical simu-
 366 lations have shown that in the initial stages of their nonlinear evolution, mirror mode
 367 waves primarily give rise to magnetic peaks which eventually, after saturation and as plasma
 368 approaches a marginally stable condition, convert to magnetic holes/dips (Hellinger et
 369 al., 2009; Ahmadi et al., 2017). Other studies suggest that mirror mode waves generate
 370 magnetic holes and peaks but only magnetic holes survive as soliton structures (Baumgärtel,
 371 1999). The magnetic peaks in Figure 8 (marked with vertical dotted lines) have smaller
 372 amplitudes than the holes and their corresponding density decrease is also small. Also
 373 note that due to low time resolution of SWIA data, density measurements exactly in-
 374 side some structures may be missing (e.g., for the depression on the second dashed line
 375 at around 12:34:10 UTC). The spatial structure of the magnetic field in the second panel
 376 of Figure 8 is most likely caused by a nonlinear saturation mechanism.

377 Although quasi-periodic depressions in panel (b) are clearly caused by mirror mode
 378 waves, not all of the components of the magnetic field approach zero at each depression,
 379 which is used as an event identification criterion by some authors (e.g., Russell et al. (2008)).
 380 At each depression there is a component of the magnetic field, in both MSO and MVA
 381 frames, that does not approach zero and sometimes increases.

382 **4.3 Isolated Magnetic Holes in the Solar Wind**

383 In Figure 9 MAVEN observations of an isolated linear MH in the solar wind are
 384 shown. The hole is 13 s long and the field depression is $\sim 84\%$. All three components of
 385 the magnetic field are negative at this time and the solar wind flow speed is ~ 432 km/s
 386 and remains unchanged throughout the event. Inside the hole, the proton density and
 387 temperature increase by about 33 and 25 percent, respectively. Temperature increase for

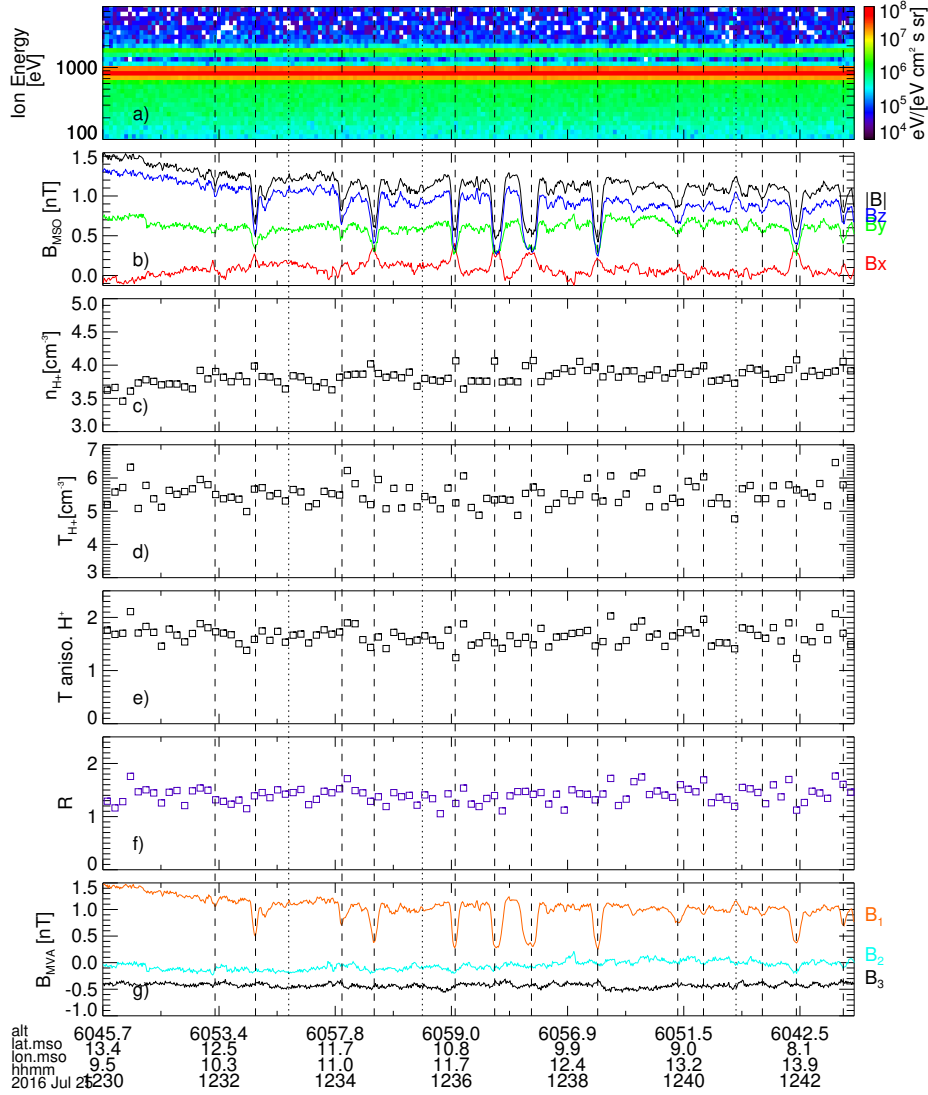


Figure 8. A train of magnetic holes in the solar wind on 25 July 2016 between 12:30:00 - 12:43:00 UTC. Panels show: (a) Ion energy spectrogram, (b) magnetic field components and magnitude in MSO coordinates, (c) proton density, (d) average proton temperature, (e) proton temperature anisotropy, (f) instability condition parameter, (g) magnetic field principal variance components. The vertical dashed and dotted lines indicate the instances of magnetic holes and peaks, respectively.

388 this event is much more noticeable than that observed for the train of holes in Figure
 389 8. Solar wind protons and alpha particles are fairly isotropic except inside the depres-
 390 sion where both anisotropies increase to above 1.5. We discussed in section 4.2 that so-
 391 lar wind plasma carrying a train of MHs is unstable to the mirror mode instability through-

392 out the entire structure. Our observations suggests that the plasma around isolated MHs
 393 becomes marginally stable or unstable only near and within the depression and it de-
 394 parts from the instability condition at other times.

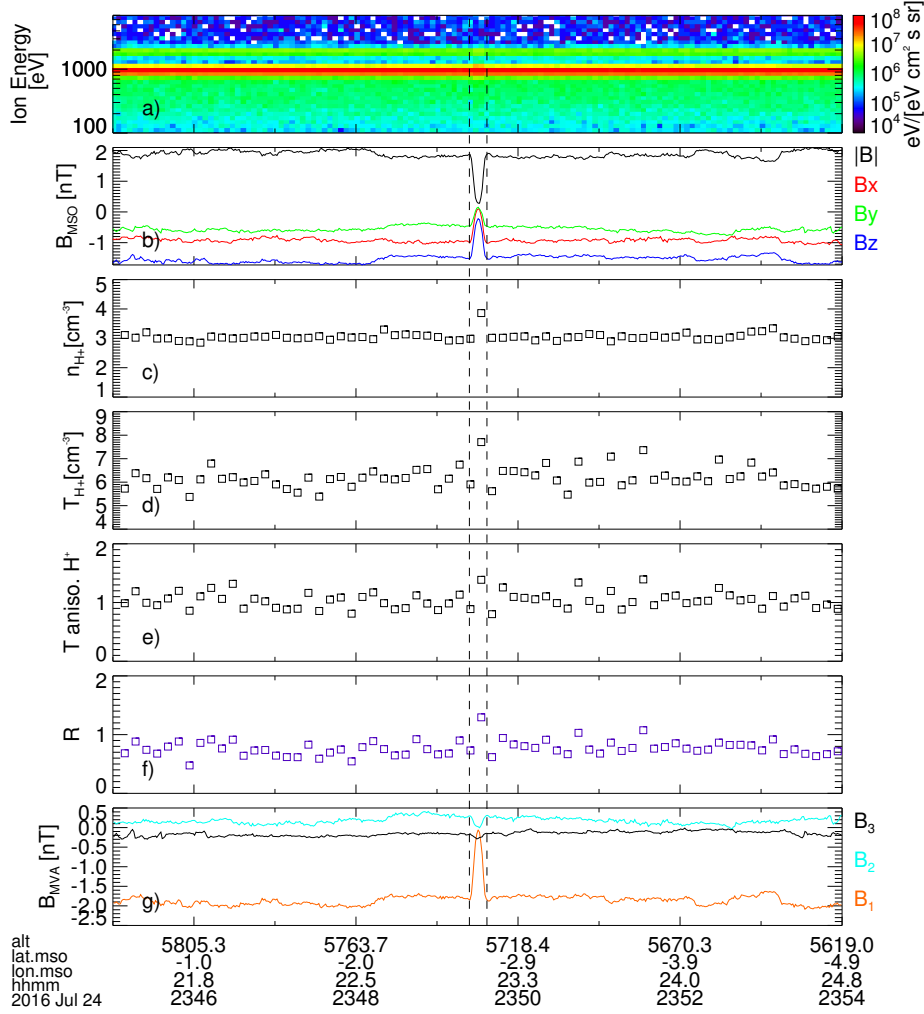


Figure 9. Similar to Figure 8 but for an isolated event on 24 July 2016. The vertical dashed lines mark the boundaries of the MH.

395 4.4 Magnetic Holes in the Extended Martian Exosphere

396 In this section, properties of MHs upstream of Mars in the presence of pickup ions
 397 are examined and main differences to MHs observed in the "pure" solar wind are iden-
 398 tified. An interesting feature that differentiates studying MHs at Mars from other places
 399 in the solar system is the extended Martian exosphere and pickup ions that are contin-

400 ously introduced in the upstream solar wind. The neutral species are normally bound
 401 by Mars' gravity unless they acquire enough escape energy that enables them to travel
 402 upstream (for comprehensive reviews of this topic readers are referred to reviews by e.g.,
 403 Lammer et al. (2008); Brain et al. (2016) and references therein). Pickup ions, mainly
 404 atomic oxygen and hydrogen ions, can be generated over a long distance upstream of the
 405 bow shock, extent of which is determined by the escape velocity of the neutral species.
 406 These ions gyrate around the IMF and form a ring-beam in the velocity distribution func-
 407 tion (VDF). Depending on the distance to Mars at the time of creation and local solar
 408 wind conditions, pickup ions can be energized to values well above the incident solar wind
 409 energy and drive significant temperature anisotropy. Figure 10 shows examples of lin-
 410 ear MHs occurring in the presence of high fluxes of heavy pickup ions on 27 August 2016
 411 between 12:50:00 - 13:00:00 UTC. During this time, the spacecraft had just crossed the
 412 terminator plane on dawn side above the northern hemisphere. Heavy pickup ions (O^+)
 413 are distinguishable in the energy spectrogram of panel (a) at energies around and above
 414 10 keV. These ions are in an early stage of their gyration. Panel (b) shows the azimuthal
 415 angle coverage of the SWIA FOV in the coarse mode. The solar wind signal is evident
 416 in $150^\circ - 200^\circ$ phi angles. The flux of non-solar wind ions in $40^\circ - 150^\circ$ angles corre-
 417 lates well with the pickup ion fluxes in panel (a). These ions lay outside the SWIA FOV
 418 in the fine mode. Ion mass spectra measured by STATIC is shown in panel (c). Fluxes
 419 in mass ranges 0.3 - 1.8 and 1.8 - 2.5 amu correspond to protons and alpha particles, re-
 420 spectively. Besides the proton and relatively weaker alpha particle fluxes, there is an ion
 421 flux at around 16 amu throughout the period. The enhanced flux above this mass be-
 422 tween 12:55:00 and 12:56:00 UTC is most likely related to O_2^+ ions. Note that at higher
 423 mass bins STATIC measurements can be highly polluted by false counts. The magnetic
 424 field components and magnitude are shown in panel (d), with two major depressions dis-
 425 tinguished at around 12:53:41 and 12:56:49 UTC. The depressions are 17 s and 21 s long,
 426 and the magnetic field rotation across the structures is $\sim 4^\circ$ and 12° , respectively. MVA
 427 analysis of the magnetic field across the depressions indicates that these structures are
 428 linearly polarized, with no indication that they are associated with a rotational dis-
 429 continuity or a reconnection current layer. Proton, alpha particle, and electron densi-
 430 ties are shown in panel (e), while panel (f) shows the temperatures of these particles. Al-
 431 pha particle densities are multiplied by a factor of 10 to match the scale of other den-
 432 sities, while their temperatures are divided by the same factor. The alpha particle den-

433 sities show enhancements inside both depressions. An electron density enhancement is
 434 particular noticeable inside the second depression at 12:56:49 UTC. The solar wind pro-
 435 ton temperature also increases significantly inside the depressions. In panel (g) we show
 436 estimates of the magnetic pressure in cyan, solar wind ion thermal pressure in orange,
 437 electron thermal pressure in black, and total pressure ($P_{tot.} = P_B + P_i + P_e$) in green.
 438 Even though there is no apparent anticorrelation between the plasma density and the
 439 magnetic field strength, nonetheless as illustrated by the green line in panel (g), the de-
 440 pressions are in pressure balance and could be associated with mirror mode instabilities.
 441 The main difference between these structures and the MHs in the pure solar wind is that
 442 the ion thermal pressure enhancement in the former is caused by increased proton tem-
 443 perature, while in the latter, it is due to increased proton density. In panel (h) of Fig-
 444 ure 10 we show that the solar wind bulk flow velocity inside the holes increases from the
 445 ambient solar wind. Plasma β s and temperature anisotropies for both protons and al-
 446 pha particles are greater than unity during this time. The plasma β s are ~ 1.5 and only
 447 increase to above 10 inside the depressions. In addition, the ion energy spectrogram in
 448 panel (a) shows enhanced fluxes of suprathermal ions at around 2 - 3 keV inside the de-
 449 pressions (yellow spots between the dashed lines). These ions enter the SWIA FOV at
 450 slightly different angles than the solar wind signal and are also seen by STATIC in the
 451 same mass range as protons. At this point, it is not clear how these ions have been ac-
 452 celerated to such high energies; however, the following sources could contribute to this
 453 population, (1) pickup hydrogen ions accelerated by the motional electric field, (2) so-
 454 lar wind protons reflected by an electric field potential across the bow shock, or (3) so-
 455 lar wind protons trapped and energized inside the mirror bubbles.

456 5 Conclusions and Implications

457 The MAVEN mission provided an opportunity to study various solar wind struc-
 458 tures at 1.5 AU. Our analysis of magnetic holes/depressions in the upstream region of
 459 Mars shows that these structures have similar shape and distributions to MHs at 1 AU.
 460 At 1.5 AU, the typical linear MH structure is asymmetrical and stretched along the mag-
 461 netic field with major to minor axis ratio of ~ 1.67 , which is about 10 percent smaller
 462 than the ratio at 1 AU (Xiao et al., 2010). The proton distributions inside the holes are
 463 anisotropic compared to the surrounding solar wind and the electron temperatures in-
 464 side the holes show a positive correlation with the depth of the depressions. We find an

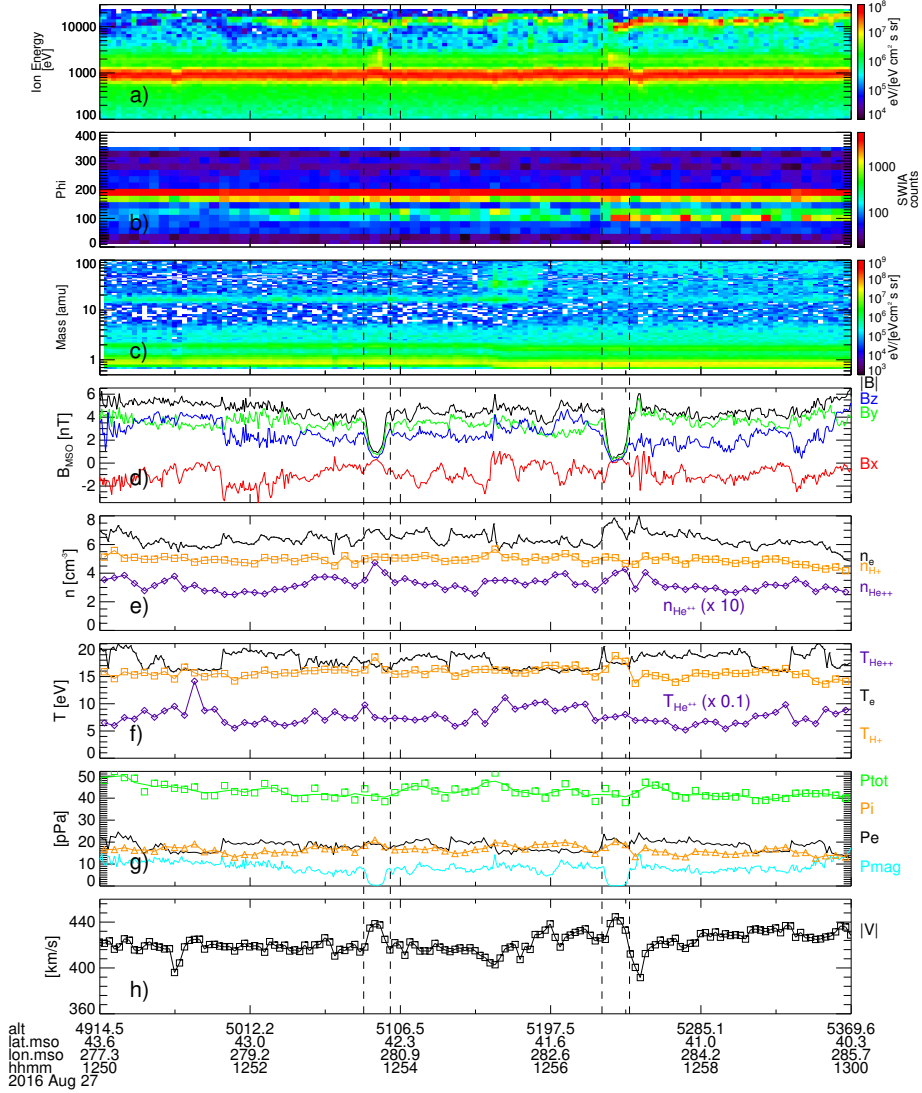


Figure 10. Magnetic hole events on 27 August 2016 accompanied by a population of heavy pickup ions. Panels show: (a) ion energy spectrogram, (b) SWIA azimuthal FOV coverage, (c) ion mass spectra measurements from STATIC (d) magnetic field components and magnitude in the MSO frame, (e) proton, alpha, and electron densities, (f) proton, alpha, and electron temperatures, (g) plasma pressure components, and (h) solar wind bulk flow speed. Alpha particle densities in panel (e) are enhanced by a factor of 10 while the temperatures in panel (f) are scaled down by a similar factor. The vertical dashed lines show the boundaries of two MHs.

465 occurrence rate of 2.1 events per day in MAVEN data using the selection criteria described
 466 in section 3. MAVEN observations reveal that linear MHs can be observed as part of a
 467 train of holes or as isolated single events. For MH trains, the solar wind plasma is un-

468 stable to mirror mode waves throughout the entire series, while isolated MHs are observed
 469 within mirror mode stable plasma, where the instability parameter R only reaches val-
 470 ues higher than the unity inside the depression. In other words, the solar wind plasma
 471 around isolated MHs could be stable outside the depression and only becomes unstable
 472 or marginally stable when the magnetic field is reduced significantly. We presented a case
 473 study of pressure-balanced linear MHs in the solar wind carrying considerable fluxes of
 474 heavy pickup ions. Data indicate that the enhancement of ion thermal pressure inside
 475 these holes is caused by an increased proton temperature, whereas for MHs in the pure
 476 solar wind the enhancement is associated with an increased plasma density (protons in
 477 particular).

478 Pickup ions introduce significant temperature anisotropy to the plasma. Besides
 479 the mirror instability, temperature anisotropy can initiate another instability mode known
 480 as the ion cyclotron instability (Gary, 1992). These two modes are in competition for
 481 the available free energy of anisotropy. While the ion cyclotron mode has a higher growth
 482 rate, in the presence of heavy ions (e.g., alpha particles,) the ion cyclotron growth rate
 483 will be suppressed significantly in favor of the mirror mode (Price et al., 1986). The MHs
 484 discussed in Figure 10 are most likely associated with mirror mode structures. It is yet
 485 to be determined whether these holes have been carried by the solar wind from smaller
 486 heliocentric distances or if they have been formed farther upstream of Mars as a result
 487 of temperature anisotropy introduced by pickup ions, and then carried to the point of
 488 observation by the solar wind. We shall compare the structure scale size for two cases,
 489 (1) a sub-interval of the mirror mode structures in the pure solar wind as shown in Fig-
 490 ure 8, and (2) a sub-interval of the structures in Figure 10 for the solar wind carrying
 491 pickup ions. The total power spectral density in the lower frequency range for each case
 492 is determined from the Morlet wavelet transform of the three components of the mag-
 493 netic field. The frequency at which spectral peaks are identified in association with the
 494 mirror mode structures are found at 0.027 Hz and 0.019 Hz corresponding to wave pe-
 495 riods of 37 s and 52 s, respectively. Using the solar wind bulk flow velocity and the back-
 496 ground magnetic field, we find the mirror mode structure size of $\sim 49 r_\rho$ for case 1, and
 497 $\sim 1.5 r_{O^+}$ for case 2. We note that in case 2 the O^+ local pickup ion gyroradius is used
 498 for scaling. The scale size would be $\sim 10.8 r_\rho$ if the enhanced proton temperatures were
 499 used instead. The mirror mode structure in case 1 is much larger than the local ion gy-
 500 roradius, and most likely not formed locally but carried by the solar wind from another

501 location. The results suggest that the structures in case 2 on 27 August could have been
 502 formed locally upstream of Mars by the heavy pickup ions. It is worth noting that sim-
 503 ilar scale size ratios have been reported for mirror mode structures formed by water group
 504 pickup ions upstream of comets (Schmid et al., 2014; Volwerk et al., 2016). In Table 1
 505 corresponding sub-intervals of the identified mirror mode structures with the associated
 506 period, solar wind conditions, gyroradius, and scale size are given.

Table 1. Identified mirror mode structure time spans with the associated period, solar wind conditions, ion gyroradius, and scale size

	July 25th	August 27th
Time interval	12:36:00 - 12:37:30	12:56:40 - 12:57:08
Mirror mode frequency (Hz)	0.027	0.019
SW velocity (km/s)	403	439.1
B_{bg} (nT)	1.3	4.9
Ion temperature (eV)	6 (H^+)	1.275×10^4 (O^+)
Local ion gyroradius (km)	$r_\rho = 273.2$	$r_{O^+} = 1.469 \times 10^4$
Mirror mode size	$49.3 r_\rho$	$1.5 r_{O^+}$

507 MAVEN orbit did not extend far beyond the bow shock (the maximum distance
 508 from the bow shock was $1.2 R_M$) and we were unable to study the evolution of MHs as
 509 they approach the bow shock. However, these structures will interact with the bow shock
 510 and propagate downstream into the magnetosheath. Plasma within MHs has a higher
 511 momentum than the ambient solar wind plasma and as they interact with the bow shock,
 512 the shock front is displaced and the inner plasma configurations of the holes also change
 513 (Grib & Leora, 2015). At planets with an intrinsic magnetosphere, such as Mercury and
 514 Earth, solar wind MHs survive the bow shock and travel through the magnetosheath in
 515 the form of diamagnetic plasmoids (Karlsson et al., 2015, 2016). At comets MHs can travel
 516 to very low altitudes while their structure becomes compressed (Plaschke et al., 2018).
 517 It is plausible for solar wind MHs to change the dynamics of the Martian magnetosphere
 518 as well. The low magnetic pressure inside MHs could also disturb the pressure balance
 519 at the induced magnetospheric boundary layer. Given the high occurrence rate of MHs
 520 at Mars (at least ~ 2.1 per day), any modulation of magnetospheric or ionospheric con-

521 conditions could have significant impacts on lower atmospheric layers in the long term. In-
 522 vestigations of impacts of magnetic holes on Mars' inner magnetosphere, ionospheric flows,
 523 and ion loss rates are left for a future follow up study.

524 Acknowledgments

525 All data presented in the figures are publicly available on the Planetary Data System
 526 (<https://pds.nasa.gov>), or can be obtained from the corresponding author. Routines for
 527 data acquisition and treatment are available through the MAVEN Toolkit publicly avail-
 528 able on the MAVEN Science Data Center (<https://lasp.colorado.edu/maven/sdc/team/pages/software.html>).
 529 We acknowledge the MAVEN contract for support. Parts of this work for the observa-
 530 tions obtained with the SWEA instrument is supported by the French space agency CNES.

531 References

- 532 Ahmadi, N., Germaschewski, K., & Raeder, J. (2017, December). Simulation
 533 of magnetic holes formation in the magnetosheath. *Physics of Plasmas*,
 534 *24*(12), 122121. Retrieved 2019-05-09, from [http://aip.scitation.org/](http://aip.scitation.org/doi/10.1063/1.5003017)
 535 [doi: 10.1063/1.5003017](http://aip.scitation.org/doi/10.1063/1.5003017)
- 536 Ala-Lahti, M. M., Kilpua, E. K. J., Dimmock, A. P., Osmane, A., Pulkkinen, T., &
 537 Souček, J. (2018, May). Statistical analysis of mirror mode waves in sheath
 538 regions driven by interplanetary coronal mass ejection. *Annales Geophysicae*,
 539 *36*(3), 793–808. Retrieved 2019-06-20, from [https://www.ann-geophys.net/](https://www.ann-geophys.net/36/793/2018/)
 540 [36/793/2018/](https://www.ann-geophys.net/36/793/2018/) [doi: 10.5194/angeo-36-793-2018](https://doi.org/10.5194/angeo-36-793-2018)
- 541 Balikhin, M. A., Pokhotelov, O. A., Walker, S. N., Boynton, R. J., & Beloff, N.
 542 (2010, March). Mirror mode peaks: THEMIS observations versus theories:
 543 MIRROR MODES PEAKS. *Geophysical Research Letters*, *37*(5), n/a–n/a.
 544 Retrieved 2019-07-23, from <http://doi.wiley.com/10.1029/2009GL042090>
 545 [doi: 10.1029/2009GL042090](http://doi.wiley.com/10.1029/2009GL042090)
- 546 Balikhin, M. A., Sibeck, D. G., Runov, A., & Walker, S. N. (2012, August). Mag-
 547 netic holes in the vicinity of dipolarization fronts: Mirror or tearing struc-
 548 tures?: DIPOLARIZATION MAGNETIC HOLES. *Journal of Geophysical Re-*
 549 *search: Space Physics*, *117*(A8), n/a–n/a. Retrieved 2019-07-23, from [http://](http://doi.wiley.com/10.1029/2012JA017552)
 550 doi.wiley.com/10.1029/2012JA017552 [doi: 10.1029/2012JA017552](https://doi.org/10.1029/2012JA017552)
- 551 Baumgärtel, K. (1999, December). Soliton approach to magnetic holes. *Journal of*

- 552 *Geophysical Research: Space Physics*, 104(A12), 28295–28308. Retrieved 2019-
 553 05-09, from <http://doi.wiley.com/10.1029/1999JA900393> doi: 10.1029/
 554 1999JA900393
- 555 Brain, D. A., Bagenal, F., Ma, Y.-J., Nilsson, H., & Stenberg Wieser, G. (2016, De-
 556 cember). Atmospheric escape from unmagnetized bodies: Atmospheric Escape:
 557 Unmagnetized Bodies. *Journal of Geophysical Research: Planets*, 121(12),
 558 2364–2385. Retrieved 2019-06-27, from [http://doi.wiley.com/10.1002/](http://doi.wiley.com/10.1002/2016JE005162)
 559 2016JE005162 doi: 10.1002/2016JE005162
- 560 Briand, C., Soucek, J., Henri, P., & Mangeney, A. (2010, December). Waves at
 561 the electron plasma frequency associated with solar wind magnetic holes:
 562 STEREO/Cluster observations: PLASMA WAVES IN MAGNETIC HOLES.
 563 *Journal of Geophysical Research: Space Physics*, 115(A12), n/a–n/a. Re-
 564 trieved 2019-05-21, from <http://doi.wiley.com/10.1029/2010JA015849>
 565 doi: 10.1029/2010JA015849
- 566 Burlaga, L. F., & Lemaire, J. F. (1978). Interplanetary magnetic holes: Theory.
 567 *Journal of Geophysical Research: Space Physics*, 83(A11), 5157–5160. Re-
 568 trieved 2019-05-09, from [https://agupubs.onlinelibrary.wiley.com/doi/](https://agupubs.onlinelibrary.wiley.com/doi/abs/10.1029/JA083iA11p05157)
 569 [abs/10.1029/JA083iA11p05157](https://agupubs.onlinelibrary.wiley.com/doi/abs/10.1029/JA083iA11p05157) doi: 10.1029/JA083iA11p05157
- 570 Burlaga, L. F., Ness, N. F., & Acuna, M. H. (2007, July). Linear magnetic holes in a
 571 unipolar region of the heliosheath observed by Voyager 1: HELIOSHEATH
 572 MAGNETIC HOLES. *Journal of Geophysical Research: Space Physics*,
 573 112(A7), n/a–n/a. Retrieved 2019-05-17, from [http://doi.wiley.com/](http://doi.wiley.com/10.1029/2007JA012292)
 574 10.1029/2007JA012292 doi: 10.1029/2007JA012292
- 575 Burlaga, L. F., Ness, N. F., & Acuña, M. H. (2006, November). Trains of mag-
 576 netic holes and magnetic humps in the heliosheath. *Geophysical Research*
 577 *Letters*, 33(21). Retrieved 2019-05-03, from [http://doi.wiley.com/10.1029/](http://doi.wiley.com/10.1029/2006GL027276)
 578 2006GL027276 doi: 10.1029/2006GL027276
- 579 Buti, B., Tsurutani, B. T., Neugebauer, M., & Goldstein, B. E. (2001, April).
 580 Generation mechanism for magnetic holes in the solar wind. *Geophysical*
 581 *Research Letters*, 28(7), 1355–1358. Retrieved 2019-05-09, from [http://](http://doi.wiley.com/10.1029/2000GL012592)
 582 doi.wiley.com/10.1029/2000GL012592 doi: 10.1029/2000GL012592
- 583 Califano, F., Hellinger, P., Kuznetsov, E., Passot, T., Sulem, P. L., & Trávníček,
 584 P. M. (2008, August). Nonlinear mirror mode dynamics: Simulations and

- 585 modeling: NONLINEAR MIRROR MODES. *Journal of Geophysical Re-*
 586 *search: Space Physics*, 113(A8), n/a–n/a. Retrieved 2019-05-10, from [http://](http://doi.wiley.com/10.1029/2007JA012898)
 587 doi.wiley.com/10.1029/2007JA012898 doi: 10.1029/2007JA012898
- 588 Chisham, G., Schwartz, S. J., Burgess, D., Bale, S. D., Dunlop, M. W., & Russell,
 589 C. T. (2000, February). Multisatellite observations of large magnetic de-
 590 pressions in the solar wind. *Journal of Geophysical Research: Space Physics*,
 591 105(A2), 2325–2335. Retrieved 2019-05-20, from [http://doi.wiley.com/](http://doi.wiley.com/10.1029/1999JA900446)
 592 [10.1029/1999JA900446](http://doi.wiley.com/10.1029/1999JA900446) doi: 10.1029/1999JA900446
- 593 Collinson, G., Halekas, J., Grebowsky, J., Connerney, J., Mitchell, D., Espley, J., ...
 594 Jakosky, B. (2015, November). A hot flow anomaly at Mars: A HOT FLOW
 595 ANOMALY AT MARS. *Geophysical Research Letters*, 42(21), 9121–9127.
 596 Retrieved 2019-06-04, from <http://doi.wiley.com/10.1002/2015GL065079>
 597 doi: 10.1002/2015GL065079
- 598 Collinson, G., Sibeck, D., Omidi, N., Grebowsky, J., Halekas, J., Mitchell, D., ...
 599 Jakosky, B. (2017, October). Spontaneous hot flow anomalies at Mars and
 600 Venus. *Journal of Geophysical Research: Space Physics*, 122(10), 9910–9923.
 601 Retrieved 2019-06-04, from [https://onlinelibrary.wiley.com/doi/abs/](https://onlinelibrary.wiley.com/doi/abs/10.1002/2017JA024196)
 602 [10.1002/2017JA024196](https://onlinelibrary.wiley.com/doi/abs/10.1002/2017JA024196) doi: 10.1002/2017JA024196
- 603 Connerney, J. E. P., Espley, J., Lawton, P., Murphy, S., Odom, J., Oliverson, R.,
 604 & Sheppard, D. (2015, December). The MAVEN Magnetic Field Inves-
 605 tigation. *Space Science Reviews*, 195(1-4), 257–291. Retrieved 2019-05-
 606 15, from <http://link.springer.com/10.1007/s11214-015-0169-4> doi:
 607 [10.1007/s11214-015-0169-4](http://link.springer.com/10.1007/s11214-015-0169-4)
- 608 Erdős, G., & Balogh, A. (1996, January). Statistical properties of mirror mode
 609 structures observed by Ulysses in the magnetosheath of Jupiter. *Journal of*
 610 *Geophysical Research: Space Physics*, 101(A1), 1–12. Retrieved 2019-05-03,
 611 from <http://doi.wiley.com/10.1029/95JA02207> doi: 10.1029/95JA02207
- 612 Fitzenreiter, R. J., & Burlaga, L. F. (1978). Structure of current sheets in mag-
 613 netic holes at 1 AU. *Journal of Geophysical Research: Space Physics*,
 614 83(A12), 5579–5585. Retrieved 2019-05-09, from [https://agupubs](https://agupubs.onlinelibrary.wiley.com/doi/abs/10.1029/JA083iA12p05579)
 615 [.onlinelibrary.wiley.com/doi/abs/10.1029/JA083iA12p05579](https://agupubs.onlinelibrary.wiley.com/doi/abs/10.1029/JA083iA12p05579) doi:
 616 [10.1029/JA083iA12p05579](https://agupubs.onlinelibrary.wiley.com/doi/abs/10.1029/JA083iA12p05579)
- 617 Fränz, M., Burgess, D., & Horbury, T. S. (2000, June). Magnetic field depressions

- 618 in the solar wind. *Journal of Geophysical Research: Space Physics*, 105(A6),
 619 12725–12732. Retrieved 2019-05-03, from [http://doi.wiley.com/10.1029/](http://doi.wiley.com/10.1029/2000JA900026)
 620 2000JA900026 doi: 10.1029/2000JA900026
- 621 Gary, S. P. (1992). The mirror and ion cyclotron anisotropy instabilities. *Journal of*
 622 *Geophysical Research*, 97(A6), 8519. Retrieved 2019-06-04, from [http://doi](http://doi.wiley.com/10.1029/92JA00299)
 623 [.wiley.com/10.1029/92JA00299](http://doi.wiley.com/10.1029/92JA00299) doi: 10.1029/92JA00299
- 624 Gary, S. P. (1993). *Theory of space plasma microinstabilities*. Cambridge:
 625 Cambridge University Press. Retrieved 2019-07-15, from [http://](http://ebooks.cambridge.org/ref/id/CB09780511551512)
 626 ebooks.cambridge.org/ref/id/CB09780511551512 doi: 10.1017/
 627 CBO9780511551512
- 628 Gary, S. P., Gosling, J. T., & Forsslund, D. W. (1981). The electromagnetic ion
 629 beam instability upstream of the Earth’s bow shock. *Journal of Geophysical*
 630 *Research*, 86(A8), 6691. Retrieved 2019-07-15, from [http://doi.wiley.com/](http://doi.wiley.com/10.1029/JA086iA08p06691)
 631 [10.1029/JA086iA08p06691](http://doi.wiley.com/10.1029/JA086iA08p06691) doi: 10.1029/JA086iA08p06691
- 632 Glassmeier, K. H., Motschmann, U., Mazelle, C., Neubauer, F. M., Sauer, K., Fuse-
 633 lier, S. A., & Acuña, M. H. (1993). Mirror Modes and Fast Magnetoacoustic
 634 Waves Near the Magnetic Pileup Boundary of Comet P/Halley. *Journal of*
 635 *Geophysical Research*, 98(A12), 20955–20964. Retrieved 2019-07-15, from
 636 <http://doi.wiley.com/10.1029/93JA02582> doi: 10.1029/93JA02582
- 637 Grib, S. A., & Leora, S. N. (2015, March). The magnetic hole as plasma in-
 638 homogeneity in the solar wind and related interplanetary medium per-
 639 turbations. *Geomagnetism and Aeronomy*, 55(2), 158–165. Retrieved
 640 2019-05-09, from <https://doi.org/10.1134/S001679321502005X> doi:
 641 10.1134/S001679321502005X
- 642 Halekas, J. S., Brain, D. A., Luhmann, J. G., DiBraccio, G. A., Ruhunusiri, S.,
 643 Harada, Y., ... Jakosky, B. M. (2017, November). Flows, Fields, and Forces
 644 in the Mars-Solar Wind Interaction: Mars-Solar Wind Interaction. *Journal*
 645 *of Geophysical Research: Space Physics*, 122(11), 11,320–11,341. Retrieved
 646 2019-06-04, from <http://doi.wiley.com/10.1002/2017JA024772> doi:
 647 10.1002/2017JA024772
- 648 Halekas, J. S., Ruhunusiri, S., Harada, Y., Collinson, G., Mitchell, D. L., Mazelle,
 649 C., ... Jakosky, B. M. (2017, January). Structure, dynamics, and sea-
 650 sonal variability of the Mars solar wind interaction: MAVEN Solar Wind

- 651 Ion Analyzer inflight performance and science results. *Journal of Geophys-*
652 *ical Research: Space Physics*, 122(1), 547–578. Retrieved 2019-06-04, from
653 <https://onlinelibrary.wiley.com/doi/abs/10.1002/2016JA023167> doi:
654 10.1002/2016JA023167
- 655 Halekas, J. S., Taylor, E. R., Dalton, G., Johnson, G., Curtis, D. W., McFadden,
656 J. P., ... Jakosky, B. M. (2015, December). The Solar Wind Ion Analyzer
657 for MAVEN. *Space Science Reviews*, 195(1-4), 125–151. Retrieved 2019-06-
658 04, from <http://link.springer.com/10.1007/s11214-013-0029-z> doi:
659 10.1007/s11214-013-0029-z
- 660 Hasegawa, A. (1969). Drift Mirror Instability in the Magnetosphere. *Physics of Flu-*
661 *ids*, 12(12), 2642. Retrieved 2019-06-04, from [https://aip.scitation.org/](https://aip.scitation.org/doi/10.1063/1.1692407)
662 [doi/10.1063/1.1692407](https://aip.scitation.org/doi/10.1063/1.1692407) doi: 10.1063/1.1692407
- 663 Hellinger, P., Kuznetsov, E. A., Passot, T., Sulem, P. L., & Trávníček, P. M. (2009,
664 March). Mirror instability: From quasi-linear diffusion to coherent structures.
665 *Geophysical Research Letters*, 36(6). Retrieved 2019-07-15, from [http://doi](http://doi.wiley.com/10.1029/2008GL036805)
666 [.wiley.com/10.1029/2008GL036805](http://doi.wiley.com/10.1029/2008GL036805) doi: 10.1029/2008GL036805
- 667 Hoppe, M. M., & Russell, C. T. (1983). Plasma rest frame frequencies and po-
668 larizations of the low-frequency upstream waves: ISEE 1 and 2 Observa-
669 tions. *Journal of Geophysical Research*, 88(A3), 2021. Retrieved 2019-
670 07-15, from <http://doi.wiley.com/10.1029/JA088iA03p02021> doi:
671 10.1029/JA088iA03p02021
- 672 Hubert, D., & Harvey, C. C. (2000, October). Interplanetary rotational discon-
673 tinuities: From the solar wind to the magnetosphere through the magne-
674 tosheath. *Geophysical Research Letters*, 27(19), 3149–3152. Retrieved
675 2019-05-10, from <http://doi.wiley.com/10.1029/2000GL003776> doi:
676 10.1029/2000GL003776
- 677 Jakosky, B. M., Lin, R. P., Grebowsky, J. M., Luhmann, J. G., Mitchell, D. F.,
678 Beutelschies, G., ... Zurek, R. (2015, December). The Mars Atmosphere
679 and Volatile Evolution (MAVEN) Mission. *Space Science Reviews*, 195(1-4),
680 3–48. Retrieved 2019-06-04, from [http://link.springer.com/10.1007/](http://link.springer.com/10.1007/s11214-015-0139-x)
681 [s11214-015-0139-x](http://link.springer.com/10.1007/s11214-015-0139-x) doi: 10.1007/s11214-015-0139-x
- 682 Joy, S. P., Kivelson, M. G., Walker, R. J., Khurana, K. K., Russell, C. T., & Pa-
683 terson, W. R. (2006, December). Mirror mode structures in the Jovian

- 684 magnetosheath. *Journal of Geophysical Research*, 111(A12). Retrieved
 685 2019-05-03, from <http://doi.wiley.com/10.1029/2006JA011985> doi:
 686 10.1029/2006JA011985
- 687 Karlsson, T., Kullen, A., Liljeblad, E., Brenning, N., Nilsson, H., Gunell, H., &
 688 Hamrin, M. (2015, September). On the origin of magnetosheath plasmoids
 689 and their relation to magnetosheath jets: ON THE ORIGIN OF MAGNE-
 690 TOSHEATH PLASMOIDS. *Journal of Geophysical Research: Space Physics*,
 691 120(9), 7390–7403. Retrieved 2019-06-04, from [http://doi.wiley.com/](http://doi.wiley.com/10.1002/2015JA021487)
 692 10.1002/2015JA021487 doi: 10.1002/2015JA021487
- 693 Karlsson, T., Liljeblad, E., Kullen, A., Raines, J. M., Slavin, J. A., & Sundberg,
 694 T. (2016, September). Isolated magnetic field structures in Mercury’s mag-
 695 netosheath as possible analogues for terrestrial magnetosheath plasmoids and
 696 jets. *Planetary and Space Science*, 129, 61–73. Retrieved 2019-05-03, from
 697 <https://linkinghub.elsevier.com/retrieve/pii/S0032063316300307>
 698 doi: 10.1016/j.pss.2016.06.002
- 699 Kivelson, M. G., & Southwood, D. J. (1996, August). Mirror instability II:
 700 The mechanism of nonlinear saturation. *Journal of Geophysical Re-*
 701 *search: Space Physics*, 101(A8), 17365–17371. Retrieved 2019-05-03, from
 702 <http://doi.wiley.com/10.1029/96JA01407> doi: 10.1029/96JA01407
- 703 Lammer, H., Kasting, J. F., Chassefière, E., Johnson, R. E., Kulikov, Y. N., & Tian,
 704 F. (2008, August). Atmospheric Escape and Evolution of Terrestrial Planets
 705 and Satellites. *Space Science Reviews*, 139(1-4), 399–436. Retrieved 2019-
 706 06-22, from <http://link.springer.com/10.1007/s11214-008-9413-5> doi:
 707 10.1007/s11214-008-9413-5
- 708 Lemaire, J., & Burlaga, L. F. (1976, December). Diamagnetic boundary layers:
 709 A kinetic theory. *Astrophysics and Space Science*, 45(2), 303–325. Re-
 710 trieved 2019-05-09, from <https://doi.org/10.1007/BF00642667> doi:
 711 10.1007/BF00642667
- 712 Liu, Y., Richardson, J. D., Belcher, J. W., & Kasper, J. C. (2007, April). Tem-
 713 perature Anisotropy in a Shocked Plasma: Mirror-Mode Instabilities in the
 714 Heliosheath. *The Astrophysical Journal*, 659(1), L65–L68. Retrieved 2019-
 715 05-03, from <http://stacks.iop.org/1538-4357/659/i=1/a=L65> doi:
 716 10.1086/516568

- 717 Lucek, E. A., Dunlop, M. W., Horbury, T. S., Balogh, A., Brown, P., Cargill, P.,
 718 ... Oddy, T. (2001). Cluster magnetic field observations in the magne-
 719 tosheath: four-point measurements of mirror structures. *Annales Geo-*
 720 *physicae*, 19(10/12), 1421–1428. Retrieved 2019-06-04, from [http://](http://www.ann-geophys.net/19/1421/2001/)
 721 www.ann-geophys.net/19/1421/2001/ doi: 10.5194/angeo-19-1421-2001
- 722 Mazelle, C., Belmont, G., Glassmeier, K.-H., Le Quéau, D., & Rème, H. (1991, Jan-
 723 uary). Ultra low frequency waves at the magnetic pile-up boundary of comet
 724 P/Halley. *Advances in Space Research*, 11(9), 73–77. Retrieved 2019-07-15,
 725 from <https://linkinghub.elsevier.com/retrieve/pii/027311779190014B>
 726 doi: 10.1016/0273-1177(91)90014-B
- 727 McFadden, J. P., Kortmann, O., Curtis, D., Dalton, G., Johnson, G., Abiad, R.,
 728 ... Jakosky, B. (2015, December). MAVEN SupraThermal and Thermal
 729 Ion Composition (STATIC) Instrument. *Space Science Reviews*, 195(1-4),
 730 199–256. Retrieved 2019-05-15, from [http://link.springer.com/10.1007/](http://link.springer.com/10.1007/s11214-015-0175-6)
 731 [s11214-015-0175-6](http://link.springer.com/10.1007/s11214-015-0175-6) doi: 10.1007/s11214-015-0175-6
- 732 Mitchell, D. L., Mazelle, C., Sauvaud, J.-A., Thocaven, J.-J., Rouzaud, J., Fedorov,
 733 A., ... Jakosky, B. M. (2016, April). The MAVEN Solar Wind Electron
 734 Analyzer. *Space Science Reviews*, 200(1-4), 495–528. Retrieved 2019-05-
 735 15, from <http://link.springer.com/10.1007/s11214-015-0232-1> doi:
 736 10.1007/s11214-015-0232-1
- 737 Neugebauer, M., Goldstein, B. E., Winterhalter, D., Smith, E. J., MacDowall, R. J.,
 738 & Gary, S. P. (2001, April). Ion distributions in large magnetic holes in the
 739 fast solar wind. *Journal of Geophysical Research: Space Physics*, 106(A4),
 740 5635–5648. Retrieved 2019-05-28, from [http://doi.wiley.com/10.1029/](http://doi.wiley.com/10.1029/2000JA000331)
 741 [2000JA000331](http://doi.wiley.com/10.1029/2000JA000331) doi: 10.1029/2000JA000331
- 742 Omidi, N., & Sibeck, D. G. (2007, January). Formation of hot flow anomalies and
 743 solitary shocks: HFAS AND SOLITARY SHOCKS. *Journal of Geophysical Re-*
 744 *search: Space Physics*, 112(A1), n/a–n/a. Retrieved 2019-06-04, from [http://](http://doi.wiley.com/10.1029/2006JA011663)
 745 doi.wiley.com/10.1029/2006JA011663 doi: 10.1029/2006JA011663
- 746 Omidi, N., Sibeck, D. G., & Blanco-Cano, X. (2009, August). Foreshock compres-
 747 sional boundary: FORESHOCK COMPRESSIONAL BOUNDARY. *Jour-*
 748 *nal of Geophysical Research: Space Physics*, 114(A8), n/a–n/a. Retrieved
 749 2019-06-06, from <http://doi.wiley.com/10.1029/2008JA013950> doi:

- 750 10.1029/2008JA013950
- 751 Omidi, N., Zhang, H., Sibeck, D., & Turner, D. (2013, January). Spontaneous hot
 752 flow anomalies at quasi-parallel shocks: 2. Hybrid simulations: HYBRID SIM-
 753 ULATIONS OF SHFAS. *Journal of Geophysical Research: Space Physics*,
 754 *118*(1), 173–180. Retrieved 2019-06-04, from [http://doi.wiley.com/](http://doi.wiley.com/10.1029/2012JA018099)
 755 [10.1029/2012JA018099](http://doi.wiley.com/10.1029/2012JA018099) doi: 10.1029/2012JA018099
- 756 Plaschke, F., Karlsson, T., Götz, C., Möstl, C., Richter, I., Volwerk, M., ... Gold-
 757 stein, R. (2018, October). First observations of magnetic holes deep within
 758 the coma of a comet. *Astronomy & Astrophysics*, *618*, A114. Retrieved 2019-
 759 05-03, from <https://www.aanda.org/10.1051/0004-6361/201833300> doi:
 760 [10.1051/0004-6361/201833300](https://www.aanda.org/10.1051/0004-6361/201833300)
- 761 Pokhotelov, O. A. (2002). Linear theory of the mirror instability in non-Maxwellian
 762 space plasmas. *Journal of Geophysical Research*, *107*(A10). Retrieved 2019-
 763 07-18, from <http://doi.wiley.com/10.1029/2001JA009125> doi: 10.1029/
 764 [2001JA009125](http://doi.wiley.com/10.1029/2001JA009125)
- 765 Price, C. P., Swift, D. W., & Lee, L.-C. (1986). Numerical simulation of nonoscil-
 766 latory mirror waves at the Earth's magnetosheath. *Journal of Geophysical Re-*
 767 *search*, *91*(A1), 101. Retrieved 2019-06-02, from [http://doi.wiley.com/10](http://doi.wiley.com/10.1029/JA091iA01p00101)
 768 [.1029/JA091iA01p00101](http://doi.wiley.com/10.1029/JA091iA01p00101) doi: 10.1029/JA091iA01p00101
- 769 Russell, C. T., Jian, L. K., Luhmann, J. G., Zhang, T. L., Neubauer, F. M., Skoug,
 770 R. M., ... Cowee, M. M. (2008, August). Mirror mode waves: Messengers
 771 from the coronal heating region. *Geophysical Research Letters*, *35*(15). Re-
 772 trieved 2019-06-06, from <http://doi.wiley.com/10.1029/2008GL034096>
 773 doi: 10.1029/2008GL034096
- 774 Russell, C. T., Riedler, W., Schwingenschuh, K., & Yeroshenko, Y. (1987, June).
 775 Mirror instability in the magnetosphere of comet Halley. *Geophysical Research*
 776 *Letters*, *14*(6), 644–647. Retrieved 2019-05-09, from [http://doi.wiley.com/](http://doi.wiley.com/10.1029/GL014i006p00644)
 777 [10.1029/GL014i006p00644](http://doi.wiley.com/10.1029/GL014i006p00644) doi: 10.1029/GL014i006p00644
- 778 Schmid, D., Volwerk, M., Plaschke, F., Vörös, Z., Zhang, T. L., Baumjohann,
 779 W., & Narita, Y. (2014, June). Mirror mode structures near Venus
 780 and Comet P/Halley. *Annales Geophysicae*, *32*(6), 651–657. Retrieved
 781 2019-06-25, from <https://www.ann-geophys.net/32/651/2014/> doi:
 782 [10.5194/angeo-32-651-2014](https://www.ann-geophys.net/32/651/2014/)

- 783 Schwartz, S. J., & Burgess, D. (1991, March). Quasi-parallel shocks: A patchwork
784 of three-dimensional structures. *Geophysical Research Letters*, *18*(3), 373–376.
785 Retrieved 2019-06-06, from <http://doi.wiley.com/10.1029/91GL00138> doi:
786 10.1029/91GL00138
- 787 Schwartz, S. J., Sibeck, D., Wilber, M., Meziane, K., & Horbury, T. S. (2006). Ki-
788 netic aspects of foreshock cavities. *Geophysical Research Letters*, *33*(12). Re-
789 trieved 2019-06-02, from <http://doi.wiley.com/10.1029/2005GL025612> doi:
790 10.1029/2005GL025612
- 791 Sibeck, D. G., Kudela, K., Mukai, T., Nemecek, Z., & Safrankova, J. (2004, Decem-
792 ber). Radial dependence of foreshock cavities: a case study. *Annales Geophys-*
793 *icae*, *22*(12), 4143–4151. Retrieved 2019-06-02, from <http://www.ann-geophys>
794 [.net/22/4143/2004/](http://www.ann-geophys.net/22/4143/2004/) doi: 10.5194/angeo-22-4143-2004
- 795 Smith, E. J. (1973, May). Identification of interplanetary tangential and rotational
796 discontinuities. *Journal of Geophysical Research*, *78*(13), 2054–2063. Retrieved
797 2019-05-20, from <http://doi.wiley.com/10.1029/JA078i013p02054> doi: 10
798 .1029/JA078i013p02054
- 799 Soucek, J., Lucek, E., & Dandouras, I. (2008, April). Properties of magnetosheath
800 mirror modes observed by Cluster and their response to changes in plasma
801 parameters: MIRROR MODE PROPERTIES. *Journal of Geophysical Re-*
802 *search: Space Physics*, *113*(A4), n/a–n/a. Retrieved 2019-05-03, from [http://](http://doi.wiley.com/10.1029/2007JA012649)
803 doi.wiley.com/10.1029/2007JA012649 doi: 10.1029/2007JA012649
- 804 Southwood, D. J., & Kivelson, M. G. (1993). Mirror instability: 1. Physical mecha-
805 nism of linear instability. *Journal of Geophysical Research*, *98*(A6), 9181. Re-
806 trieved 2019-05-28, from <http://doi.wiley.com/10.1029/92JA02837> doi: 10
807 .1029/92JA02837
- 808 Sperveslage, K., Neubauer, F. M., Baumgärtel, K., & Ness, N. F. (2000).
809 Magnetic holes in the solar wind between 0.3 AU and 17 AU. *Nonlin-*
810 *ear Processes in Geophysics*, *7*(3/4), 191–200. Retrieved 2019-06-04,
811 from <http://www.nonlin-processes-geophys.net/7/191/2000/> doi:
812 10.5194/npg-7-191-2000
- 813 Stevens, M. L., & Kasper, J. C. (2007, May). A scale-free analysis of magnetic
814 holes at 1 AU: MAGNETIC HOLES AT 1 AU. *Journal of Geophysical Re-*
815 *search: Space Physics*, *112*(A5), n/a–n/a. Retrieved 2019-05-03, from [http://](http://doi.wiley.com/10.1029/2006JA012649)

- 816 doi.wiley.com/10.1029/2006JA012116 doi: 10.1029/2006JA012116
- 817 Szegö, K., Glassmeier, K.-H., Bingham, R., Bogdanov, A., Fischer, C., Haeren-
818 del, G., ... Zank, G. (2000, December). Physics of Mass Loaded Plasmas.
819 *Space Science Reviews*, 94(3), 429–671. Retrieved 2018-09-08, from [https://](https://doi.org/10.1023/A:1026568530975)
820 doi.org/10.1023/A:1026568530975 doi: 10.1023/A:1026568530975
- 821 Tajiri, M. (1967, June). Propagation of Hydromagnetic Waves in Collisionless
822 Plasma. II. Kinetic Approach. *Journal of the Physical Society of Japan*,
823 22(6), 1482–1494. Retrieved 2019-06-04, from [http://journals.jps.jp/doi/](http://journals.jps.jp/doi/10.1143/JPSJ.22.1482)
824 [10.1143/JPSJ.22.1482](http://journals.jps.jp/doi/10.1143/JPSJ.22.1482) doi: 10.1143/JPSJ.22.1482
- 825 Trotignon, J., Mazelle, C., Bertucci, C., & Acuña, M. (2006, April). Mar-
826 tian shock and magnetic pile-up boundary positions and shapes deter-
827 mined from the Phobos 2 and Mars Global Surveyor data sets. *Plan-*
828 *etary and Space Science*, 54(4), 357–369. Retrieved 2019-06-04, from
829 <https://linkinghub.elsevier.com/retrieve/pii/S0032063306000110>
830 doi: 10.1016/j.pss.2006.01.003
- 831 Tsurutani, B. T. (2002). Relationship between discontinuities, magnetic holes,
832 magnetic decreases, and nonlinear Alfvén waves: Ulysses observations
833 over the solar poles. *Geophysical Research Letters*, 29(11). Retrieved
834 2019-05-31, from <http://doi.wiley.com/10.1029/2001GL013623> doi:
835 10.1029/2001GL013623
- 836 Tsurutani, B. T., Dasgupta, B., Galvan, C., Neugebauer, M., Lakhina, G. S., Ar-
837 ballo, J. K., ... Buti, B. (2002, December). Phase-steepened Alfvén waves,
838 proton perpendicular energization and the creation of magnetic holes and
839 magnetic decreases: The ponderomotive force: THE PONDEROMOTIVE
840 FORCE. *Geophysical Research Letters*, 29(24), 86–1–86–4. Retrieved
841 2019-05-15, from <http://doi.wiley.com/10.1029/2002GL015652> doi:
842 10.1029/2002GL015652
- 843 Tsurutani, B. T., Guarnieri, F. L., Echer, E., Lakhina, G. S., & Verkhoglyadova,
844 O. P. (2009, August). Magnetic decrease formation from <1 AU to ~5 AU:
845 Corotating interaction region reverse shocks: MAGNETIC DECREASE FOR-
846 MATION. *Journal of Geophysical Research: Space Physics*, 114(A8), n/a–n/a.
847 Retrieved 2019-06-04, from <http://doi.wiley.com/10.1029/2008JA013927>
848 doi: 10.1029/2008JA013927

- 849 Tsurutani, B. T., Lakhina, G. S., Verkhoglyadova, O. P., Echer, E., Guarnieri, F. L.,
 850 Narita, Y., & Constantinescu, D. O. (2011, February). Magnetosheath and
 851 heliosheath mirror mode structures, interplanetary magnetic decreases, and
 852 linear magnetic decreases: Differences and distinguishing features: REVIEW.
 853 *Journal of Geophysical Research: Space Physics*, *116*(A2), n/a–n/a. Retrieved
 854 2019-05-03, from <http://doi.wiley.com/10.1029/2010JA015913> doi:
 855 10.1029/2010JA015913
- 856 Tsurutani, B. T., Southwood, D. J., Smith, E. J., & Balogh, A. (1992, June). Non-
 857 linear magnetosonic waves and mirror mode structures in the March 1991
 858 Ulysses interplanetary event. *Geophysical Research Letters*, *19*(12), 1267–1270.
 859 Retrieved 2019-05-21, from <http://doi.wiley.com/10.1029/92GL00782> doi:
 860 10.1029/92GL00782
- 861 Turner, J. M., Burlaga, L. F., Ness, N. F., & Lemaire, J. F. (1977, May). Mag-
 862 netic holes in the solar wind. *Journal of Geophysical Research*, *82*(13),
 863 1921–1924. Retrieved 2019-05-03, from <http://doi.wiley.com/10.1029/JA082i013p01921> doi: 10.1029/JA082i013p01921
- 865 Volwerk, M., Richter, I., Tsurutani, B., Götz, C., Altwegg, K., Broiles, T., ... Glass-
 866 meier, K.-H. (2016, January). Mass-loading, pile-up, and mirror-mode waves
 867 at comet 67p/Churyumov-Gerasimenko. *Annales Geophysicae*, *34*(1), 1–15.
 868 Retrieved 2018-02-23, from <https://www.ann-geophys.net/34/1/2016/> doi:
 869 10.5194/angeo-34-1-2016
- 870 Winterhalter, D., Neugebauer, M., Goldstein, B. E., Smith, E. J., Bame, S. J.,
 871 & Balogh, A. (1994). Ulysses field and plasma observations of magnetic
 872 holes in the solar wind and their relation to mirror-mode structures. *Jour-
 873 nal of Geophysical Research*, *99*(A12), 23371. Retrieved 2019-05-03, from
 874 <http://doi.wiley.com/10.1029/94JA01977> doi: 10.1029/94JA01977
- 875 Winterhalter, D., Neugebauer, M., Goldstein, B. E., Smith, E. J., Tsurutani, B. T.,
 876 Bame, S. J., & Balogh, A. (1995, April). Magnetic holes in the solar wind
 877 and their relation to mirror-mode structures. *Space Science Reviews*, *72*(1-2),
 878 201–204. Retrieved 2019-06-04, from [http://link.springer.com/10.1007/
 879 BF00768780](http://link.springer.com/10.1007/BF00768780) doi: 10.1007/BF00768780
- 880 Winterhalter, D., Smith, E. J., Neugebauer, M., Goldstein, B. E., & Tsurutani,
 881 B. T. (2000, June). The latitudinal distribution of solar wind mag-

- 882 netic holes. *Geophysical Research Letters*, *27*(11), 1615–1618. Retrieved
883 2019-05-03, from <http://doi.wiley.com/10.1029/1999GL003717> doi:
884 10.1029/1999GL003717
- 885 Wu, C. S., & Davidson, R. C. (1972, October). Electromagnetic instabilities pro-
886 duced by neutral-particle ionization in interplanetary space. *Journal of Geo-*
887 *physical Research*, *77*(28), 5399–5406. Retrieved 2019-05-21, from [http://doi](http://doi.wiley.com/10.1029/JA077i028p05399)
888 [.wiley.com/10.1029/JA077i028p05399](http://doi.wiley.com/10.1029/JA077i028p05399) doi: 10.1029/JA077i028p05399
- 889 Xiao, T., Shi, Q. Q., Zhang, T. L., Fu, S. Y., Li, L., Zong, Q. G., ... Reme, H.
890 (2010, September). Cluster-C1 observations on the geometrical structure of
891 linear magnetic holes in the solar wind at 1 AU. *Annales Geophysicae*, *28*(9),
892 1695–1702. Retrieved 2019-05-03, from [http://www.ann-geophys.net/28/](http://www.ann-geophys.net/28/1695/2010/)
893 [1695/2010/](http://www.ann-geophys.net/28/1695/2010/) doi: 10.5194/angeo-28-1695-2010
- 894 Zhang, T. L., Russell, C. T., Baumjohann, W., Jian, L. K., Balikhin, M. A., Cao,
895 J. B., ... Vörös, Z. (2008, May). Characteristic size and shape of the mir-
896 ror mode structures in the solar wind at 0.72 AU: SOLAR WIND MIRROR
897 MODE STRUCTURES. *Geophysical Research Letters*, *35*(10). Retrieved
898 2019-05-03, from <http://doi.wiley.com/10.1029/2008GL033793> doi:
899 10.1029/2008GL033793
- 900 Zhang, T. L., Russell, C. T., Zambelli, W., Vörös, Z., Wang, C., Cao, J. B., ...
901 Glassmeier, K.-H. (2008, December). Behavior of current sheets at directional
902 magnetic discontinuities in the solar wind at 0.72 AU. *Geophysical Research*
903 *Letters*, *35*(24). Retrieved 2019-05-03, from [http://doi.wiley.com/10.1029/](http://doi.wiley.com/10.1029/2008GL036120)
904 [2008GL036120](http://doi.wiley.com/10.1029/2008GL036120) doi: 10.1029/2008GL036120
- 905 Zurbuchen, T. H., Hefti, S., Fisk, L. A., Gloeckler, G., Schwadron, N. A., Smith,
906 C. W., ... Burlaga, L. F. (2001). On the origin of microscale mag-
907 netic holes in the solar wind. *Journal of Geophysical Research: Space*
908 *Physics*, *106*(A8), 16001–16010. Retrieved 2019-05-09, from [https://](https://agupubs.onlinelibrary.wiley.com/doi/abs/10.1029/2000JA000119)
909 agupubs.onlinelibrary.wiley.com/doi/abs/10.1029/2000JA000119 doi:
910 10.1029/2000JA000119